First principles study on structure and superionic transition of bismuth oxides

Akifumi Matsumoto

Department of Materials Science and Engineering,

Kyoto University, Sakyo, Kyoto 606-8501, Japan

Contents

Part I

General introduction

Oxygen ionic conductor is one of a functional material in which O ions diffuse in the solid phase as fast as in the liquid phase. Besides the conductivity of O ions, oxygen ionic conductor allows only O ions to pass through the body. Making use of these features, oxygen ionic conductor is applied or expected to be applied to various applications (e.g., oxygen sensor, oxygen pump, electrolyte of solid oxide fuel cells, etc.).[1] Various materials have been reported to show oxygen ion-conducting. Figure 1 shows the oxygen ionic conductivity of various oxygen ionic conductors.[2] Among these various oxygen ionic conductors, Bismuth oxide, Bi_2O_3, -based system has the highest ionic conductivity.

Bi_2O_3 has been reported to exhibit six polymorphs, α, β, γ, δ, ε and ω phases.[3-12] α-Bi_2O_3 has a monoclinic structure and is stable at room temperature and atmospheric pressure. It is transformed to δ-Bi_2O_3 upon heating to above 1000 K, which is stable up to its melting point.[3-10] β- and γ-Bi_2O_3 are obtained as metastable phases during the cooling of δ-Bi_2O_3.[3,4,7-9] ε-Bi_2O_3 can be obtained by hydrothermal treatment in highly concentrated KOH solution,[11] and which is irreversibly transformed to the α-form at 673 K. ω-Bi_2O_3 has been prepared on a BeO substrate.[12]

Figure 2 shows the conductivity of pure Bi_2O_3 on heating and cooling. The transitions in Bi_2O_3 are attended by sudden changes in the electrical conductivity.[9,13] On heating, the transition from α-Bi_2O_3 to δ-Bi_2O_3 occurs at approximately 1000 K and the conductivity increase by several orders of magnitude. It is known that this high conductivity in δ-Bi_2O_3 is due to the conduction of O ions. On cooling, β-Bi_2O_3 and

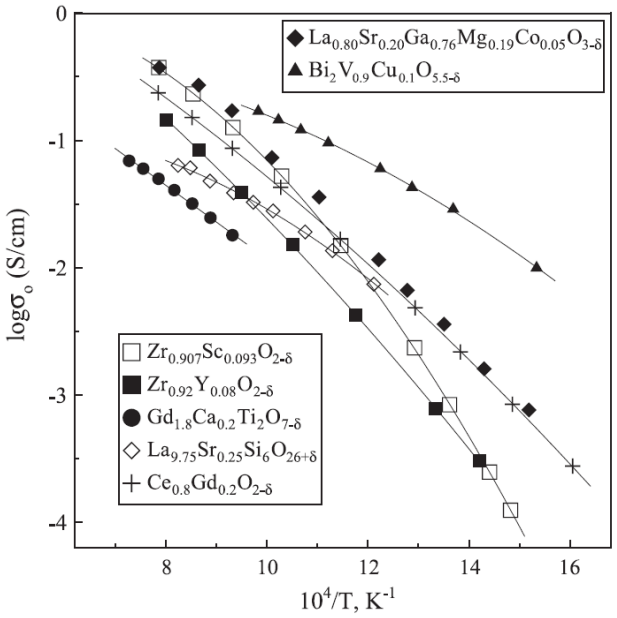

FIG. 1. The Arrhenius plot of the conductivity of various oxygen ionic conductors.[2]

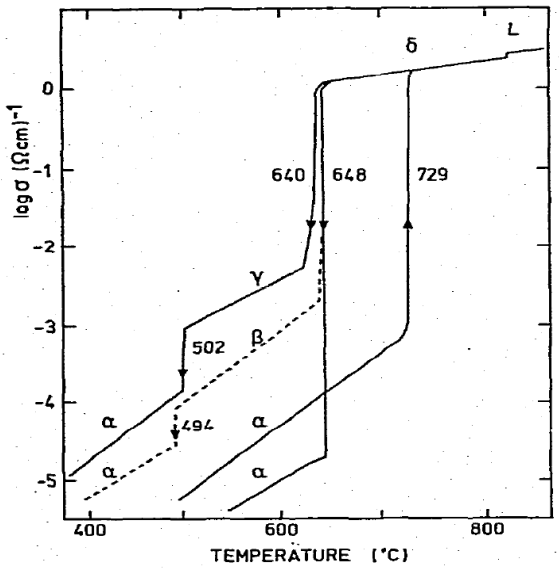

FIG. 2. The conductivity of Bi_2O_3.[9] The measurements are performed with various conditions and the representative results are shown. On cooling, solid and broken lines are obtained by the measurements from the liquid state and compressed powder specimen, respectively. β phase is obtained with a cooling rate of 33 K/min at approximately 648 °C. γ phase is obtained with a cooling rate of 0.1 K/min at approximately 640 °C.

γ-Bi_2O_3 appears at the cooling rate of 33 K/min and 0.1 K/min, respectively. With this transition, the conductivity decrease considerably. Only the high-temperature phase, δ-Bi_2O_3, exhibits high oxide ionic conductivity of more than 1 S/cm as shown in Fig. 2. This conductivity is almost 2 orders higher than a commonly used yttira stabilized zirconia at comparable temperatures. However the stable temperature region of δ-Bi_2O_3 is so narrow that prevent applying this material to applications. In order to improve the stability of ion-conducting phase or understand the mechanism of ionic conduction, various investigations have been performed on Bi_2O_3.

δ-Bi_2O_3 was reported to have a defective fluorite structure: Bi ions occupy the 4*a* sites at (0, 0, 0), forming a face-centered-cubic sublattice, and oxide ions occupy the 8*c* sites at (1/4, 1/4, 1/4), forming a simple cubic sublattice. Since the Bi ions are trivalent, a quarter of the O sites are vacant to ensure charge neutrality. This high concentration of intrinsic vacant sites provides a simple explanation for the high conductivity of the O ions. Therefore, numerous experimental and computational studies have been performed on the arrangement of oxide ions and vacant sites in the O sublattice.[5,6,14-27] Sillen suggested that the vacant sites were ordered along the <111> direction on the basis of powder X-ray diffraction measurements on quenched samples.[5] Gattow and Schröder reported that no ordering was observed in the O sublattice upon performing high-temperature powder X-ray diffraction.[6] Since then, the arrangement of vacant sites has been assumed to be random. Also, the oxide ions were reported to be off-centered from the ideal sites in the fluorite structure according to recent neutron diffraction experiments.[14-16] Theoretical approaches have been also performed on Bi_2O_3. However, since the structure of δ-Bi_2O_3 can not be determined uniformly, the calculation is not as easy as in other oxides. In this work, we aimed to get over such difficulties and provide the information about the structural features of Bi_2O_3. The relationships of defective fluorite family are investigated by first-principles calculations.

In Part II, it is shown that various local minimum structures exist in defective fluorite Bi_2O_3 (df-Bi_2O_3) and the conventional geometry optimization can lead a wrong structure. Thus, a series of dynamically stable structures of the df-Bi_2O_3 is searched by first-principles lattice dynamics calculations. The crystal symmetry is lowered and local distortion is included systematically along imaginary modes of lattice vibrations. A clear band gap appears when local distortion is included in this way, which is consistent with experimental results. Many theoretical calculations in the past indicated metallic or semimetallic electronic structures. The appropriate inclusion of the symmetry breaking and local distortion are therefore essential in reproducing the electronic structures of Bi_2O_3. Three stable structures, β, η and ε' phase, are obtained in this method. It is suggested that these structures are ordered low-temperature polymorphs of the disordered δ-Bi_2O_3 in the defective fluorite-Bi_2O_3 family.

In Part III, the dynamically stable structures are found in the same procedure of Part II for df-As_2O_3 and df-Sb_2O_3. As and Sb belong the same group of Bi, 15 group, in the Periodic table. They are also known to form sesquioxides. In these sesquioxides, cation is considered as trivalent and ns electrons remain at the valence band. The effect of these so-called "lone pair electrons" on the stability in M_2O_3 (M = As, Sb, Bi) is discussed. It is indicated that the localization of ns electrons is more remarkable in the dynamically stable structures compared with dynamically unstable structures for these sesquioxides. Thus, it can be thought that the stability of these sesquioxides is influenced significantly by the effect of lone pair electrons as well as the electrostatic interaction.

In Part IV, first-principles molecular dynamics calculations are done on df-Bi_2O_3 family to see the movement of O ions at various temperatures. cubic-β phase is found to maintain its atomic arrangement at higher temperature compared with other df-Bi_2O_3. Although the calculational conditions are statistically insufficient, the

estimated diffusion coefficient is not so different from the experimental value. The volume of the cell influences the ion-conduction. It is shown that larger lattice parameter promotes ion-conduction. According to this result, sulfur is substituted into O sites to expand the volume. The sulfur doped cubic-β phase shows order-disorder transition at lower temperature than pure cubic-β phase. Although sulfur also diffuse in this system and the suggested system is not desirable for applications, these calculations are thought to be helpful for search a practical material of Bi_2O_3-based system.

References

[1] P. Knauth and H. L. Tuller, J. Am. Ceram. Soc., **85,** 1654 (2002).

[2] V. V. Kharton, F. M. B. Marques and A. Atkinson, Solid State Ionics, **174,** 135 (2004).

[3] M. Drache, P. Roussel, and J. Wignacourt, Chem. Rev. **107,** 80 (2007).

[4] N. M. Sammes, G. A. Tompsett, H. Näfe, and F. Aldinger, J. Eur. Ceram. Soc. **19,** 1801 (1999).

[5] L. G. Sillen, Ark. Kemi **12A,** 1 (1937).

[6] V. G. Gattow and H. Schröder, Z. Anorg. Allg. Chem. **318,** 176 (1962).

[7] V. G. Gattow and D. Schutze, Z. Anorg. Allg. Chem. **328,** 44 (1964).

[8] E. M. Levin and R. S. Roth, J. Res. Natl. Bur. Stand. **68A,** 197 (1964).

[9] H. A. Harwig and A. G. Gerards, Thermochim. Acta **28,** 121 (1979).

[10] C. N. R. Rao, G. V. S. Rao, and S. Ramdas, J. Phys. Chem. **73,** 672 (1969).

[11] N. Cornei, N. Tancret, F. Abraham, and O. Mentré, Inorg. Chem. Commun. **45,** 4886 (2006).

[12] A. F. Gualtieri, S. Imovilli, and M. Prudenziati, Powder Diffr. **12,** 90 (1997).

[13] T. Takahashi, H. Iwahara, and Y. Nagai, J. Appl. Electrochem. **2,** 97 (1972).

[14] P. D. Battle, C. R. A. Catlow, J. Drennan, and A. D. Murray, J. Phys. C: Solid State Phys. **16,** L561 (1983).

[15] M. Yashima and D. Ishimura, Chem. Phys. Lett. **378,** 395 (2003).

[16] S. Hull, S. T. Norberg, M. G. Tucker, S. G. Eriksson, C. E. Mohn and S. Stølen, Dalton Trans., 8737 (2009)

Part II

Structures and energetics of Bi_2O_3 polymorphs in a defective fluorite family derived by systematic first principles lattice dynamics calculations

1. INTROCUCTION

As described in Part I, various experimental investigations have been done on Bi_2O_3. To elucidate the structure of δ-Bi_2O_3 and the nature of its high ionic conductivity by theoretical approaches, several studies using first-principles calculations based on density functional theory (DFT) have been reported.[1-11] A unit cell of the simplest defective fluorite structure contains eight O sites, of which two are vacant. In the present study, this unit cell will be hereafter referred to as the single unit cell. The term "array" will be used to distinguish the arrangement of vacant sites in the O sublattice. On the other hand, the term "arrangement" will retain its general meaning and refer to a set of specific atomic positions. There are three possible arrays of the vacant sites in the single unit cell. They are aligned along either the <100>, <110> or <111> direction, as schematically shown in Fig. 3. Theoretical calculations on df-Bi_2O_3 with the three different vacancy arrays formed for the single unit cell have been performed in many studies.

Medvedeva *et al.* first reported first-principles calculations of df-Bi_2O_3 using the linear muffin-tin orbital (LMTO) method with the local density approximation

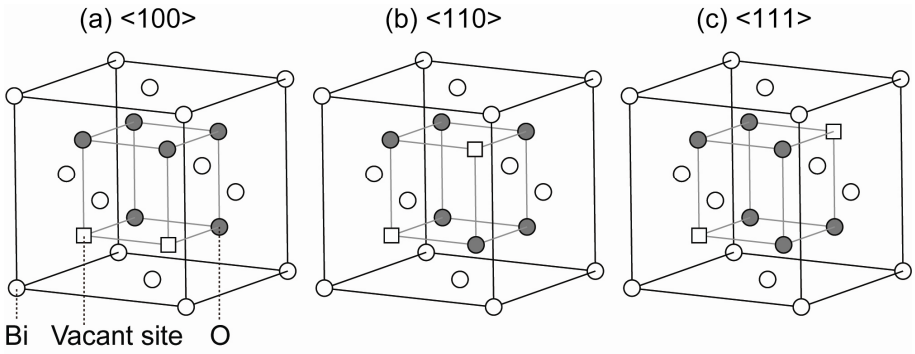

FIG. 3. Three possible arrays of the vacant sites in a single unit cell, aligned along the (a) <100>, (b) <110> and (c) <111> directions. White spheres, gray spheres and white squares denote Bi, O and vacant sites, respectively.

(LDA).[1] They suggested that an arrangement in the <111> array (a <111> arrangement) had a metallic electronic structure and was more stable than a <110> arrangement.

Carlsson *et al.* reported first-principles calculations of α- and df-Bi_2O_3 using the plane-wave basis ultrasoft-pseudopotential method with the generalized gradient approximation (GGA).[2] They suggested that a <100> arrangement was the most stable among the three arrangements with different vacancy arrays, and that its energy was 0.80 eV/f.u. (f.u.: formula unit) higher than that of α-Bi_2O_3. In the electronic structure of the <100> arrangement, the top of the valence band had a higher energy than the bottom of the conduction band, indicating a semimetallic electronic structure. Walsh *et al.* also reported similar results for first-principles calculations using the projector augmented wave (PAW) method with the GGA.[3] Their <100> and <110> arrangements were semimetallic, while the <111> arrangement was metallic. The <100> arrangement was the most stable among the three arrangements and had a higher energy than α-Bi_2O_3 by 0.74 eV/f.u. Experimentally, δ-Bi_2O_3 exhibits a clear band gap of 1.73 eV[12].

Since this was obtained in a nanocrystalline thin-film sample, the band gap of the perfect crystalline δ-Bi_2O_3 may be larger than 1.73 eV. However, all the above calculations indicated semimetallic or metallic electronic structures. Zhong *et al.* considered spin-orbit coupling as a relativistic effect in the Bi ions using the full-potential linearized augmented plane-wave (FLAPW) method with the GGA.[7] They reported that a <110> arrangement had a band gap of 0.46 eV and was the most stable among the three arrangements. They suggested that the spin-orbit coupling effect was an important factor in determining the size of the band gap. However, their <111> arrangement was still metallic.

Recently, calculations on df-Bi_2O_3 beyond the single unit cell, i.e., the df-Bi_2O_3 superstructure have been reported. Aidhy *et al.* found an arrangement having lower energy than those in the single-unit-cell models when a 2×2×2 superstructure was examined by a combination of classical molecular dynamics (MD) simulations and PAW calculations with the GGA.[4] Music *et al.* reported that some arrangements of the 2×2×2 superstructure were lower in energy than the <100> arrangement using the ultrasoft-pseudopotential method with the GGA.[9] They confirmed that the arrangement reported by Aidhy *et al.* was the lowest in energy. Mohn *et al.* reported that there were many arrangements of the 2×2×2 superstructure lower in energy than the three single-unit-cell models on the basis of first-principles MD simulations and lattice statics calculations combined with powder neutron diffraction experiments.[10,11] They suggested that the distribution of the oxide ions surrounding the Bi ions was highly asymmetric.

In spite of the past extensive studies on Bi_2O_3, two major issues remain. 1) The electronic structure, particularly the band gap, is inconsistent with experimental results; the three simple arrangements within the single unit cell are semimetallic or metallic. The experimentally obtained band gap of δ-Bi_2O_3 is 1.73 eV.[12] 2) The theoretical energy of df-Bi_2O_3 relative to α-Bi_2O_3 has not been conclusively determined.

Both Carlsson *et al.* and Walsh *et al.* reported that their <100> arrangement is ~0.7 eV/f.u. higher in energy than α-Bi_2O_3. Using superstructure models, Mohn *et al.*[11] recently reported the presence of low-energy structures that are more than 0.13 eV/f.u. higher in energy than α-Bi_2O_3. As will be shown later, these structures are not the lowest-energy arrangements within the given array.

Carlsson *et al.* performed a series of first-principles calculations to examine the energy barrier of df-Bi_2O_3 between <111> and <100> arrangements via a <110> arrangement by displacing an oxide ion. They found no energy barrier for the transformation from <111> to <110>. Although the result is not quantitatively reliable since they did not include the probable relaxation of the structure during the transformation, it appears that the <111> arrangement is not stable against lattice dynamics. Therefore, we investigate the lattice dynamics of each structure. In this part, we will show that the reported structures are dynamically unstable and that symmetry breaking and local distortion around Bi ions are essential for describing the atomic and electronic structures of Bi_2O_3 with a defective fluorite structure. The local distortion leads to a wide band gap of 2 to 3 eV. It also considerably reduces the energy even though the array is not changed. The lowest energy relative to α-Bi_2O_3 is found to be $0.07 - 0.08$ eV/f.u. We show three different examples of such low-energy structures, all of which are stable with respect to the lattice dynamics.

2. COMPUTATIONAL METHOD

The first-principles calculations were performed by the PAW method[13] implemented in the VASP code.[14-16] Plane waves were used as the basis functions with a cutoff energy of 360 eV. The convergence of the formation energy with respect to the

plane-wave cutoff was found to be better than 0.01 eV/f.u. The radii of the PAW potentials were 1.32 and 0.98 Å for Bi and O, respectively. The 5*d*, 6*s* and 6*p* electrons for Bi and the 2*s* and 2*p* electrons for O were treated as valence and the remaining electrons were kept frozen. The exchange-correlation term was treated with the Perdew-Burke-Ernzerhof (PBE) functional based on the generalized gradient approximation (GGA)[17]. Both the unit cell of the fluorite structure and the 2×2×2 supercell were used for df-Bi_2O_3. Integration in the reciprocal space was performed by the Monkhorst-Pack scheme using a 4×4×4 mesh for the single unit cell, a 2×2×2 mesh for the 2×2×2 supercell and a 3×2×2 mesh for α-Bi_2O_3. The total energy was minimized until the energy convergence became less than 1×10^{-5} eV. The stability of the model structures against lattice dynamics was examined as described in the following sections. The force-constant approach involving a finite displacement was used for this purpose by employing the *fropho* code.[18-20] The 2×2×2 supercells were used with a displacement of 0.01 Å along the *x*, *y* and *z* directions for each atom.

3. RESULTS

A. α-Bi_2O_3 and the three arrangements within the single unit cell for df-Bi_2O_3

α-Bi_2O_3 and the three arrangements of Bi_2O_3 with the single unit cell are examined in this section. Their atomic and electronic structures are described with a review of similar works in the literature.[1-3] The optimized structure of α-Bi_2O_3 is summarized in Table 1. The lattice constants and internal positions are in good agreement with experimental results.[21] α-Bi_2O_3 exhibits the electronic band structure shown in Fig. 4 with a band gap of 2.29 eV. The gap is 0.2 eV smaller than that obtained

by experiments.[22] This underestimation is within the expected range of the GGA error. The three arrangements for df-Bi_2O_3 were constructed simply by locating the Bi and oxide ions in the ideal positions of the fluorite structure, and the structures were optimized while maintaining the initial symmetry. The symmetry, optimized structural data and energy relative to α-Bi_2O_3 are summarized in Table 2. The electronic band structures are illustrated in Fig. 5. The <100> arrangement has the lowest energy among the three arrangements. However, it has a higher energy than α-Bi_2O_3 by 0.73 eV/f.u. The energy difference among the three arrangements and α-Bi_2O_3 is in quantitatively good agreement with those in the literature.[3] Both the <100> and <110> arrangements have a gap between the valence and conduction bands. However, the valence band tops are above the conduction band bottoms. Hence, these two arrangements are semimetallic. In contrast, the Fermi energy intersects the bands in the <111> arrangement, indicating that the <111> arrangement is metallic.

Lattice dynamics calculations are performed on the three arrangements. Figure 6 illustrates the phonon band structures of the <100>, <110> and <111>

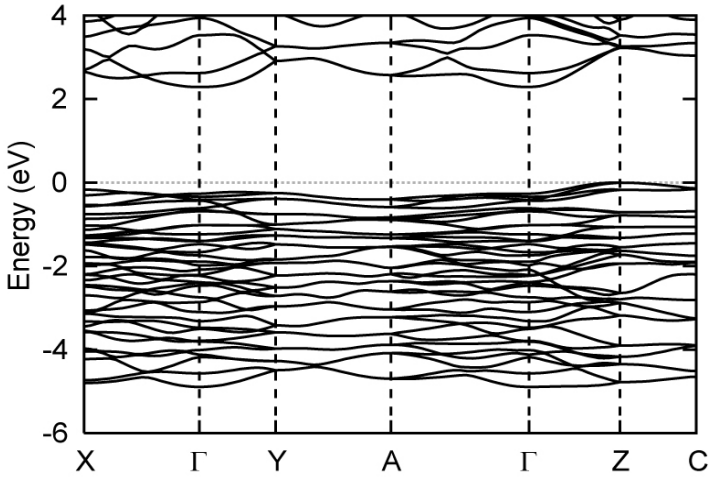

FIG. 4. Electronic band structure of α-Bi_2O_3. The top of the valence band is set to 0 on the vertical axis.

TABLE 1. Details of calculated structure, Bi-O bond length and band gap of α-Bi_2O_3. The values in parenthesis were obtained from experiments (Ref. 21 and 22).

				α-Bi_2O_3				
Space Group				$P2_1/c$ (No. 14)				
Lattice Parameter				a = 5.93Å (5.84 Å) b = 8.28Å (8.15 Å) c = 7.54Å (7.50 Å) β = 113° (113°)				
Atom Coordinate	Bi (1)	4*e*	0.524	0.184	0.366	(0.523	0.184	0.362)
	Bi (2)	4*e*	0.040	0.041	0.777	(0.040	0.043	0.776)
	O (1)	4*e*	0.778	0.298	0.707	(0.777	0.304	0.707)
	O (2)	4*e*	0.235	0.052	0.125	(0.235	0.048	0.127)
	O (3)	4*e*	0.270	0.031	0.512	(0.269	0.028	0.511)
Bond Length (Å)	Bi(1)-O(1)					2.24 × 1		
						2.58 × 1		
	Bi(1)-O(2)					2.21 × 1		
	Bi(1)-O(3)					2.12 × 1		
						2.50 × 1		
	Bi(2)-O(1)					2.23 × 1		
						2.53 × 1		
	Bi(2)-O(2)					2.15 × 1		
						2.41 × 1		
	Bi(2)-O(3)					2.29 × 1		
						2.80 × 1		
Band Gap (eV)				2.29 (2.5)				

TABLE 2. Details of structure, Bi-O bond length and energy relative to α-Bi_2O_3 of the three arrangements in the single unit cell for df-Bi_2O_3.

	<100>					<110>				
Space Group	$P4_2/mcm$ (No. 132)					$P\bar{4}m2$ (No. 115)				
Lattice Parameter	a = 5.84Å c = 5.72Å					a = 3.92 Å ($\sqrt{2}$ a = 5.54 Å) c = 5.85 Å				
Atom Coordinate	Bi (1)	4*i*	0.736	0.736	0	Bi (1)	2*g*	0	0.5	0.777
	O (1)	4*e*	0	0.5	0.25	O (1)	1*a*	0	0	0
	O (2)	2*d*	0.5	0.5	0.25	O (2)	1*b*	0.5	0.5	0
						O (3)	1*d*	0	0	0.5
Bond Length (Å)	Bi (1) – O (1)			2.42 × 2		Bi (1) – O (1)			2.35 × 2	
	Bi (1) – O (2)			2.51 × 4		Bi (1) – O (2)			2.35 × 2	
						Bi (1) – O (3)			2.54 × 2	
Relative Energy (eV/f.u.)	0.73					0.85				

	<111>				
Space Group	$Pn\bar{3}m$ (No. 224)				
Lattice Parameter	a = 5.59 Å				
Atom Coordinate	Bi (1)	4*b*	0.25	0.25	0.25
	O (1)	6*d*	0	0.5	0.5
Bond Length (Å)	Bi (1) – O (1)			2.42 × 6	
Relative Energy (eV/f.u.)	1.85				

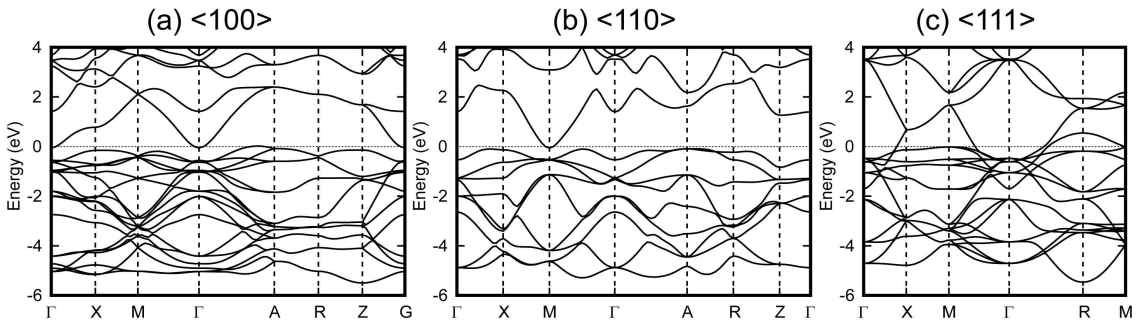

FIG. 5. Electronic band structures of the three arrangements in the single unit cell for df-Bi_2O_3 shown in Table 2. The top of the valence band is set to 0 on the vertical axis.

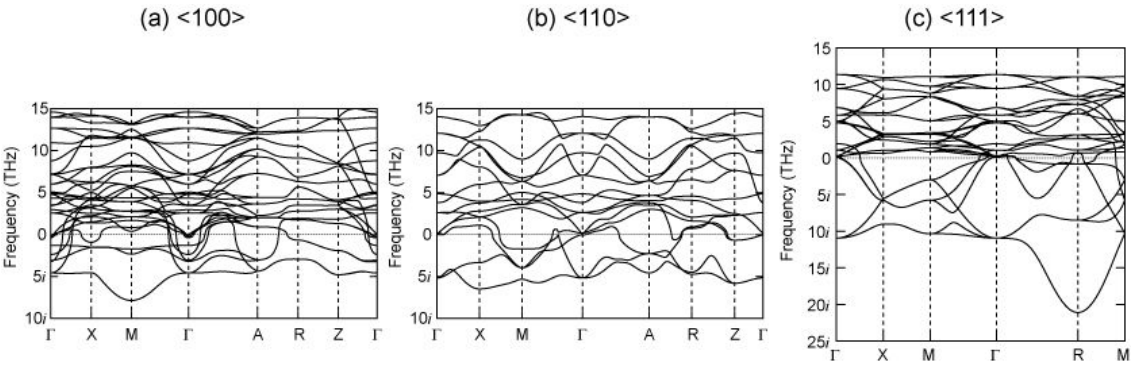

FIG. 6. Phonon band structures of the three arrangements in the single unit cell for df-Bi_2O_3 shown in Table 2.

arrangements computed in the present study. Note that the phonon dispersion curves are shown with the notation of the wave vectors in the corresponding unit cells, since each arrangement has a different symmetry and size of the unit cell. The imaginary value of the frequency illustrated below 0 indicates that the structure is at a local maximum of the potential surface and is unstable against the corresponding lattice vibration. All three arrangements have vibration modes with imaginary frequency at any point in the first Brillouin zone (BZ).

B. Symmetry breaking and local distortion in <111> array model

In this section, we investigate the dynamically stable structure of the <111> vacancy-array model, which exhibits a metallic electronic structure and the highest energy, as described in the previous section. First, a new structure is constructed by introducing a displacement of ~0.5 Å along the eigenvector of the imaginary vibration mode at the Γ point (0, 0, 0) in Fig. 6(c). The set of atomic displacements is schematically shown in Fig. 7. This is the set of displacements that can be included in the single unit cell. As will be shown later, the description of the set of displacements corresponding to the other points in the BZ such as the R point (1/2, 1/2, 1/2) requires the use of a supercell. The structural parameters are optimized after introducing the set of displacements. Note that both the new arrangement and the original arrangement are included in the <111> array model. However, the symmetry is lower in the new arrangement. We will hereafter call the original and new arrangements the high-symmetry (HS) and low-symmetry (LS) arrangements, respectively.

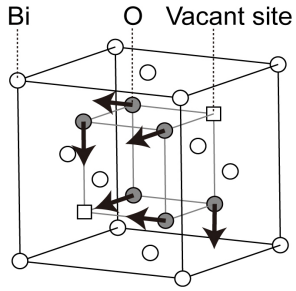

FIG. 7. Schema of the eigenvectors of the imaginary vibration mode at the Γ point (0,0,0) in the <111> model (see also Fig. 6(c)). The displacement of Bi atoms is much less than that of O atoms. The directions of the vibration of O atoms are almost parallel to the Cartesian axes.

TABLE 3. Details of structure, Bi-O bond length, energy relative to α-Bi_2O_3 and band gap of <111>-LS arrangement of df-Bi_2O_3.

	<111>-LS				
Space Group	*R*3*m* (No. 160)				
Lattice Parameter	*a* = 5.78Å *α* = 88.8°				
Atom Coordinate	Bi (1)	3*b*	0.522	0.030	0.522
	Bi (2)	1*a*	0.000	0.000	0.000
	O (1)	3*b*	0.265	0.656	0.265
	O (2)	3*b*	0.763	0.158	0.763
Bond Length (Å)	Bi(1)-O(1)			2.14 × 2	
				3.07 × 1	
	Bi(1)-O(2)			2.15 × 1	
				2.95 × 2	
	Bi(2)-O(1)			2.92 × 3	
	Bi(2)-O(2)			2.14 × 3	
Relative Energy (eV/f.u.)	0.39				
Band Gap (eV)	2.37				

The displacement in the <111>-HS arrangement leads to *R*3*m* space group symmetry. The optimized structural data of the <111>-LS arrangement is summarized in Table 3. The symmetry breaking causes a local distortion around Bi ions. The Bi-O bond length is constant at 2.42 Å in the HS arrangement, whereas it varies in the range of 2.14−3.07 Å in the LS arrangement. This variation of the Bi-O bond length should be preferred by Bi^{3+}, since α-Bi_2O_3 also has a variable bond length, ranging from 2.12 to 2.80 Å. The symmetry breaking and local distortion leads to a marked change in the electronic structure. Figure 8 illustrates the electronic band structure of the <111>-LS arrangement. There is a band gap of 2.37 eV, which is in strong contrast to the metallic

structure of the <111>-HS arrangement shown in Fig. 5(c). The <111>-LS arrangement is lower in energy than the <111>-HS arrangement by 1.46 eV/f.u. These results imply that the inclusion of the symmetry breaking and local distortion is essential to describe the atomic and electronic structures of df-Bi_2O_3. The constraint of imposing too high symmetry should lead to an incorrect electronic structure with too high energy.

Although the energy of the <111>-LS arrangement is significantly lower than that of the <111>-HS arrangement, an additional phonon calculation for the <111>-LS arrangement found that a small imaginary frequency remains at the L point (1/2, 0, 1/2) of the unit cell of the <111>-LS arrangement, which corresponds to the X point (1/2, 0, 0) in the notation of the original primitive cell shown in Fig. 6(c). This implies that the current <111>-LS arrangement is not a dynamically stable structure.

To examine wave vectors other than the Γ point in Fig. 6(c), we need to construct supercell models. The supercells will hereafter be denoted by their sizes compared with the single unit cell. Since we employed the 2×2×2 supercell for the phonon calculations, we considered only the wave vectors commensurate with the periodicity of the supercell. These wave vectors will be hereafter referred to as "commensurate points". Atomic displacements that correspond to the imaginary vibration mode having the largest absolute value (or the strongest imaginary frequency) are chosen. For the <111>-HS arrangement, the strongest imaginary frequency appears at the R point (1/2, 1/2, 1/2) in Fig. 6(c), and the new arrangement requires a 2×2×2 supercell as the unit cell. The displacement leads to a structure with the space group $Fd\bar{3}m$. The structure is optimized by imposing the $Fd\bar{3}m$ symmetry. We will hereafter call the newer arrangement the <111>-LS(2×2×2) arrangement, whose structural data is summarized in Table 4. Interestingly, the <111>-LS(2×2×2) arrangement is isostructural to arsenolite, As_2O_3, and senarmontite, Sb_2O_3. Its band gap is 2.59 eV, which is larger than that of the <111>-LS arrangement. The <111>-LS(2×2×2) arrangement is lower in

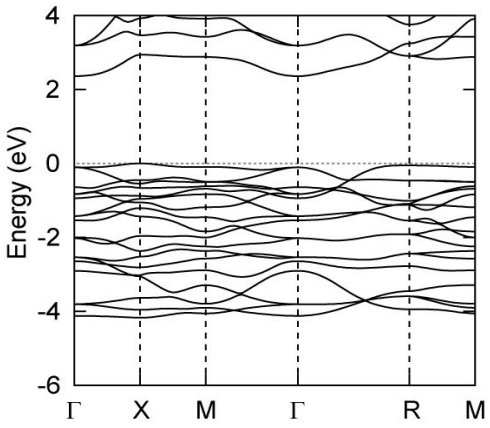

FIG. 8. Electronic band structure of <111>-LS arrangement of df-Bi_2O_3 shown in Table 3. The top of the valence band is set to 0 on the vertical axis.

energy than the <111>-LS arrangement by 0.10 eV/f.u. It does not exhibit dynamical instabilities at the commensurate points according to the results of phonon calculations. In the following section, however, we will see that there are more stable arrangements of df-Bi_2O_3 than the <111>-LS(2×2×2) arrangement.

TABLE 4 Details of structure, Bi-O bond length, energy relative to α-Bi_2O_3 and band gap of <111>-LS(2×2×2) arrangement of df-Bi_2O_3.

			<111>-LS(2×2×2)		
Space Group			$Fd\bar{3}m$ (No. 227)		
Lattice Parameter			a = 11.41Å		
Atom Coordinate	Bi (1)	32*e*	0.370	0.370	0.370
	O (1)	48*f*	0.200	0	0
Bond Length (Å)	Bi (1) – O (1)			2.14 × 3	
				2.86 × 3	
Relative Energy (eV/f.u.)			0.29		
Band Gap (eV)			2.59		

C. Symmetry breaking and local distortion in <100> array model

Symmetry breaking in the <100> array model is also examined within the 2×2×2 supercell. Similar to the case of the <111>-LS(2×2×2) model, a set of atomic displacements is initially made toward the eigenvector of the strongest imaginary frequency. The displacements correspond to the M point (1/2, 1/2, 0) in Fig. 4(a), which leads to the structure of the space group $P4_2/nmc$ with a $\sqrt{2}\times\sqrt{2}\times1$ supercell as the unit cell. After the structure optimization with the space group $P4_2/nmc$, a weak imaginary frequency remains at the Γ point (0, 0, 0). Optimization eventually leads to the <100>-LS(2×2×2) arrangement with the space group $P\bar{4}2_1c$, which does not exhibit dynamical instabilities at the commensurate points. The structural data, Bi-O bond length, band gap and energy relative to α-Bi_2O_3 for this arrangement are summarized in Table 5. The relative energy of the <100>-LS(2×2×2) arrangement is only 0.08 eV/f.u. It is very interesting that the <100>-LS(2×2×2) arrangement obtained in this way is

isostructural to the experimentally obtained β-Bi_2O_3 structure determined by a neutron diffraction experiment.[23] β-Bi_2O_3 is known to be formed at 920 K during the cooling of δ-Bi_2O_3[24] or by the decomposition of $Bi_2O_2CO_3$ at 650 K.[23] The experimentally obtained transition enthalpy between α- and β-Bi_2O_3 was reported to be 0.08 or 0.09 eV/f.u.[24,25] It is therefore natural that β-Bi_2O_3 appears in the present study as one of the lowest-energy forms. The experimental lattice parameters of β-Bi_2O_3 are a = 7.739 and c = 5.636 Å. The theoretical values are 3 and 1% larger than the experimental values, which are within the GGA error. The internal parameters are also in good agreement with each other. We can therefore identify the <100>-LS(2×2×2) arrangement to be β-Bi_2O_3. The <100>-LS(2×2×2) arrangement exhibits a band gap of 1.75 eV.

TABLE 5. Details of structure, and Bi-O bond length, energy relative to α-Bi_2O_3 and band gap of <100>-LS(2×2×2) arrangement of df-Bi_2O_3.

	<100>-LS(2×2×2)				
Space Group	$P\bar{4}2_1c$ (No. 114)				
Lattice Parameter	a = 7.98 Å c = 5.71 Å				
Atom Coordinate	Bi (1)	8*e*	-0.029	0.261	0.247
	O (1)	4*d*	0	0.5	0.414
	O (2)	8*e*	0.321	0.288	-0.052
Bond Length (Å)	Bi (1) – O (1)			2.14 × 1	
	Bi (1) – O (2)			2.70 × 1	
				2.15 × 1	
				2.33 × 1	
				2.39 × 1	
				3.28 × 1	
Relative Energy (eV/f.u.)	0.08				
Band Gap (eV)	1.75				

D. Symmetry breaking and local distortion in <110> array model

The same procedure as that described in the previous section is also carried out for <110> array model. The <110>-HS arrangement has the strongest imaginary phonon frequency at the X point (1/2, 0, 0) shown in Fig. 6(b), which leads to the structure of the space group *Pmm*2 with a √2×1/√2×1 supercell as the unit cell. After the structure optimization with this space group, an imaginary frequency remains at the Y point (0, 1/2, 0). Optimization leads to another *Pmm*2 structure with a √2×√2×1 supercell as the unit cell with a relative energy of 0.53 eV/f.u. and a band gap of 1.40 eV. However, the imaginary mode does not disappear. The procedure then requires a structure of the space group *Fmm*2 with a 2√2×2√2×2 supercell as the unit cell. The calculation leads to a structure with a relative energy of 0.35 eV/f.u and a band-gap of 1.83 eV. However, atomic displacements in this structure during the geometry optimization are too large for the position of the O atoms to be maintained in the <110> array model. The imaginary mode does not disappear even in this model. Further symmetry break calculations were not attempted. In conclusion, no dynamically stable arrangement for <110> model within the 2×2×2 supercell was found by the procedure adopted in the present study.

E. Symmetry breaking and local distortion in other array models of superstructures

Recently, several groups reported that other vacancy-array models with the 2×2×2 superstructure exhibit lower energy than the three simple array models as described above. Two kinds of vacancy arrays of the superstructure are therefore studied in this section to search for low-energy arrangements. First, a bixbyite-type vacancy

array is examined. The bixbyite structure is also called a C-rare-earth structure and is typical of sesquioxides such as Y_2O_3, In_2O_3 and Mn_2O_3. This structure belongs to the space group $Ia\bar{3}$ and can be considered as another vacancy-array model formed in the 2×2×2 superstructure. The phonon band structure of the bixbyite-type Bi_2O_3 (bixbyite-HS) arrangement exhibits imaginary vibration modes. The symmetry breaking according to the imaginary mode at the H point (1, 0, 0) leads to the $Pa\bar{3}$ space group (bixbyite-LS) with a unit cell of the same size. The optimized structural data, bond length, energy and band gap are summarized in Table 6 for both HS and LS. The symmetry breaking reduces the energy to 0.07 eV/f.u., which is as low as the energy of β-Bi_2O_3. The low-energy structure that Aidhy *et al.* reported has a space group of $Fm\bar{3}$,[4] which can be classified into the bixbyite-type vacancy array in our terminology. This is the same array as that Music *et al.* referred to as the combined <110> and <111> oxygen-vacancy ordering.[9] Although they did not report the relative energy of their structures with respect to α-Bi_2O_3, their structures may be the same as the bixbyite-HS arrangement judging from the energy relative to other df-Bi_2O_3 arrangements. Mohn *et al.* also reported a structure with the same vacancy array as this one, and referred to it as a <111> + <110> structure.[11] They reported many structures that have relative energies lower than the bixbyite-HS arrangement. However they clearly have higher energies than the bixbyite-LS arrangement found in the present study. Aidhy *et al.* also suggested that their bixbyite-HS arrangement can be stabilized by including local distortion,[5] although they have reported neither detailed structure nor energy gain after the structure optimization. The reported structure may be another local minimum structure within the bixbyite-type vacancy array. Although the polymorph that corresponds to the bixbyite-LS arrangement has not been reported experimentally, it is likely to be formed during the cooling of δ-Bi_2O_3, similar to the case of β-Bi_2O_3. We hereafter call the bixbyite-LS arrangement η-Bi_2O_3.

TABLE 6. Details of structure, Bi-O bond length and energy relative to α-Bi_2O_3 of bixbyite-HS and -LS arrangements of df-Bi_2O_3.

			bixbyite-HS					bixbyite-LS		
Space Group			$Ia\bar{3}$ (No. 206)					$Pa\bar{3}$ (No. 205)		
Lattice Parameter			a = 11.21Å					a = 11.42Å		
Atom Coordinate	Bi (1)	8*b*	0.25	0.25	0.25	Bi (1)	8*c*	0.255	0.255	0.255
	Bi (2)	24*d*	0.973	0	0.25	Bi (2)	24*d*	0.977	-0.009	0.259
	O (1)	48*e*	0.622	0.104	0.154	O (1)	24*d*	0.618	0.087	0.135
						O (2)	24*d*	0.104	0.636	0.681
Bond Length (Å)	Bi(1)-O(1)		2.43 × 6			Bi(1)-O(1)		2.78 × 3		
						Bi(1)-O(2)		2.20 × 3		
	Bi(2)-O(1)		2.30 × 2			Bi(2)-O(1)		2.14 × 1		
			2.41 × 2					2.29 × 1		
			2.56 × 2					2.61 × 1		
						Bi(2)-O(2)		2.24 × 1		
								2.53 × 1		
								3.08 × 1		
Relative Energy (eV/f.u.)			0.28					0.07		
Band Gap (eV)			1.94					2.66		

The second vacancy-array superstructure model considered is constructed by analogy to the orthorhombic Sb_2O_3 crystal known as valentinite. Note that the structure of valentinite belongs to the space group *Pccn*, which is the same as that of metastable ε-Bi_2O_3 reported in the literature.[26] This is a structure derived from the <100> vacancy-array model. The unit cell with the [001] array is doubled in the [100] direction, which is accompanied by a translation of the vacancy array by half of the unit cell parameter in the [010] direction. The highest-symmetry arrangement of this vacancy array has the space group *Ibam*, and it has an imaginary vibration mode at the Γ point (0, 0, 0). Following the procedure described above, the valentinite-LS arrangement with the space group *Pbcn* was obtained. The optimized structure data, bond length, relative energy and band gap are summarized in Table 7. The valentinite-LS arrangement has a relative energy of 0.07 eV/f.u. and does not exhibit dynamical instabilities at any commensurate point. Since the space group of valentinite-LS is *Pbcn*, which is slightly different from that of ε-Bi_2O_3, *Pccn*, reported experimentally, the valentinite-LS arrangement is referred to as ε'-Bi_2O_3. Here is another example showing that the consideration of symmetry breaking and local distortion are essential.

TABLE 7. Details of structure, Bi-O bond length and energy relative to α-Bi_2O_3 of valentinite-LS arrangement of df-Bi_2O_3.

			valentinite-LS		
Space Group			*Pbcn* (No. 60)		
Lattice Parameter			*a* = 11.81Å *b* = 5.74 Å *c* = 5.69 Å		
Atom Coordinate	Bi (1)	8*d*	0.128	0.309	0.550
	O (1)	4*c*	0	0.444	0.25
	O (2)	8*d*	0.715	0.090	0.112
Bond Length (Å)	Bi(1)-O(1)			2.36 × 1	
	Bi(1)-O(2)			2.41 × 1	
				2.12 × 1	
				2.26 × 1	
				2.42 × 1	
				3.52 × 1	
Relative Energy (eV/f.u.)			0.07		
Band Gap (eV)			2.22		

F. Magnitude of the zero-point vibration energy of four low-energy structures

Once the phonon dispersion curves are obtained, one can evaluate the magnitude of the zero-point vibration energy (ZPE), E_{ZP}, for the given structure within the harmonic approximation. The vibrational density of states is found to be not significantly different between the three low-energy structures of df-Bi_2O_3 (<100>-LS(2×2×2), bixbyite-LS, valentinite-LS) and α-Bi_2O_3. Consequently, E_{ZP} for the four structures are almost the same, ranging from 0.21 to 0.22 eV/f.u. In other words, the difference in the ZPE among the four structures is smaller than 0.01 eV/f.u. The contribution of the ZPE therefore does not change the energetic hierarchy of these structures.

4. DISCUSSION

A. Atomic pair distribution in members of the df-Bi_2O_3 family

In the previous section, we reported that the symmetry breaking and local distortion are essential for obtaining dynamically stable and low-energy structures. To analyze the nature of the local distortion, the pair distributions for Bi-O, Bi-Bi and O-O are examined. Figure 9 summarizes the results for the three low-energy structures in comparison with that for α-Bi_2O_3. To examine the effect of the symmetry breaking, results for higher-symmetry arrangements of the <100> array model, i.e., <100>-HS and <100>-$P4_2/nmc$, are compared with that for the <100>-LS(2×2×2) arrangement. It can be observed that the Bi-O pair distribution becomes evenly distributed upon lowering the symmetry, thereby lowering the energy. A similar tendency can be seen for the O-O

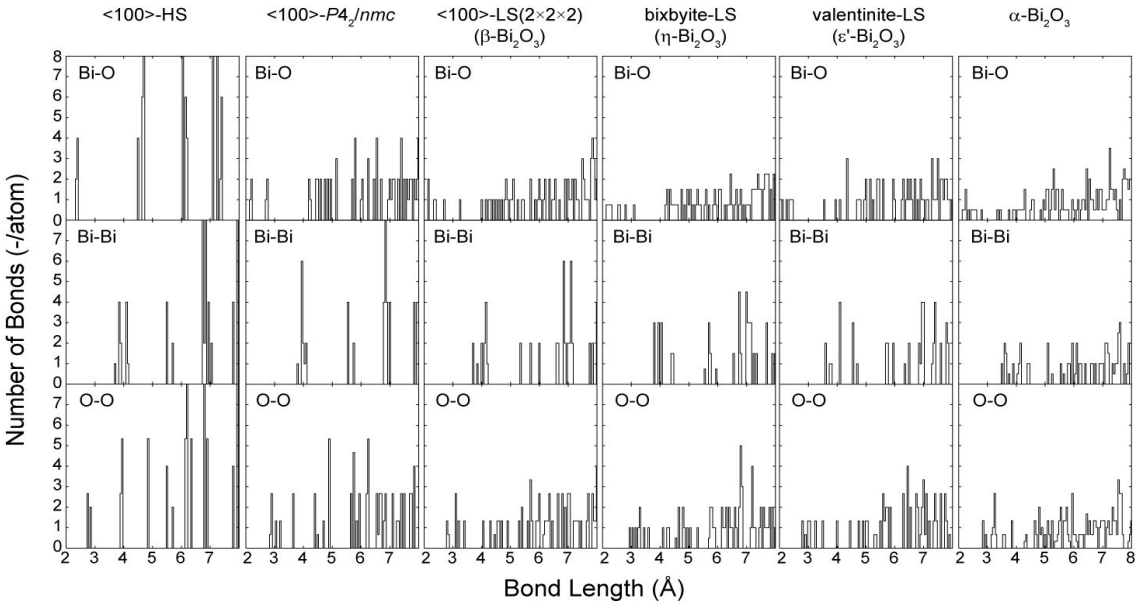

FIG. 9. Atomic pair distributions of Bi-O, Bi-Bi and O-O in two high-symmetry arrangements of the <100> array, and those of the three stable arrangements of df-Bi_2O_3, and α-Bi_2O_3.

pair distribution. On the other hand, the Bi-Bi pair distribution is less evenly distributed, even in the low-energy structures. The results imply that the symmetry breaking and local distortion have a larger impact on the O sublattice than on the Bi sublattice. In other words, the O sublattice is more vulnerable to the local distortion.

B. Electronic band gap of members of the df-Bi_2O_3 family

In experiments δ-Bi_2O_3 exhibits a clear band gap of 1.73 eV.[12] On the other hand, most previous theoretical calculations gave semimetallic or metallic electronic structures for the three simple arrays within the single unit cell of df-Bi_2O_3. We found that a clear band gap appears, even in the three vacancy-array models for df-Bi_2O_3, only when the

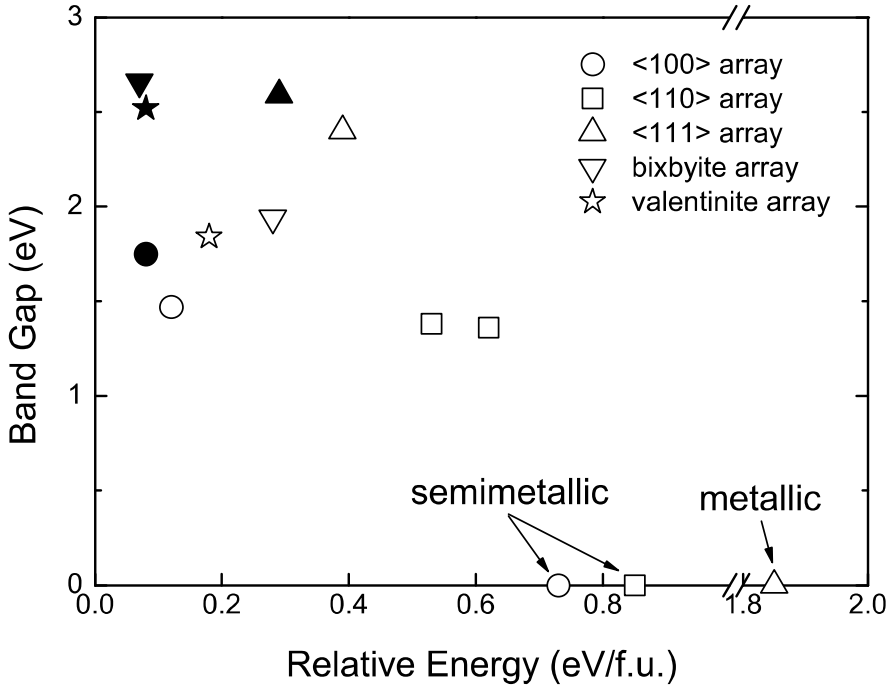

FIG. 10. Relation between band gap and energy relative to α-Bi_2O_3 for each vacancy-array model. Array models are distinguished by the shape of marks. The open marks correspond to the dynamically unstable arrangements, and the solid marks correspond to the dynamically stable LS arrangements.

local distortion is appropriately included. Figure 10 shows the relationship between the GGA band gap and the relative energy. Array models are distinguished by the shape of marks in Fig. 10. The open marks correspond to the dynamically unstable arrangements, and the solid marks correspond to the dynamically stable LS arrangements. There is a clear trend of the band gap decreasing with increasing relative energy for each vacancy array. The results imply that semimetallic or metallic electronic structures of df-Bi_2O_3 are artifacts due to the selection of structures with too high energy to be realized under ordinary conditions.

C. Discussion on δ-Bi_2O_3 showing high oxide ionic conduction

Among the polymorphs of Bi_2O_3, δ-Bi_2O_3 is the only phase with high oxide ionic conductivity of more than 1 S/cm. A working hypothesis has been proposed that δ-Bi_2O_3 is the disordered phase in the df-Bi_2O_3 family and that the disordering plays a central role in the high oxide ionic conductivity. Experimentally, δ-Bi_2O_3 is known to be transformed to β-Bi_2O_3 during cooling. Although β-Bi_2O_3 is a member of the df-Bi_2O_3 family, it does not exhibit high oxide ionic conductivity. The δ to β transition at 923 K was found to be accompanied by a sudden change in the electrical conductivity and a transition enthalpy of 0.23 eV/f.u. The high intrinsic concentration of the vacant O sites alone cannot be a sufficient condition for the high oxide ionic conductivity.

Assuming that vacant sites in the O sublattice in δ-Bi_2O_3 is random, the primary contribution to the free-energy difference at the transition between δ and β is the configurational entropy, ΔS, which can be evaluated to be $\Delta S = -k_B$ (1/4 ln 1/4 + 3/4 ln 3/4) = 2.25 k_B, where k_B is the Boltzmann constant. The contribution, $T\Delta S$, is 0.18 eV/f.u. at T = 923 K, which is in reasonable agreement with the experimentally obtained transition enthalpy ΔH for δ–β, i.e., ΔH = 0.23 eV/f.u. at 923 K. On the basis of experimental data obtained by thermal analysis, Harwig and Gerards[24] reported that the degree of disorder in δ-Bi_2O_3, estimated by the relative entropy gain for the α–δ transition, is comparable to that in liquid Bi_2O_3. These facts support the idea that δ-Bi_2O_3 is the disordered phase in the df-Bi_2O_3 family.

According to the present theoretical study, the three ordered phases, namely, β-Bi_2O_3 (<100>-LS(2×2×2)), ε'-Bi_2O_3 (valentinite-LS) and η-Bi_2O_3 (bixbyite-LS), have relative formation energies of 0.07 to 0.08 eV/f.u., which is very close to the experimentally obtained transition enthalpy for α–β, i.e., 0.08 to 0.09 eV/f.u.[24,25] Although neither the δ–ε' transition nor the δ–η transition has been experimentally

observed, it may be possible to realize them under appropriate experimental conditions.

5. SUMMARY

To search for a series of dynamically stable structures of df-Bi_2O_3, first-principles lattice dynamics calculations were systematically performed. Atomic arrangements were relaxed along imaginary modes of lattice vibrations in three vacancy-array models in the single unit cell and two vacancy-array models in the 2×2×2 superstructure. The structures and energetics of low-energy structures were comprehensively discussed. The major results of this part can be summarized as follows:

1) Within the <111> array model, the <111>-LS(2×2×2) arrangement was found to be dynamically stable with an energy of 0.29 eV/f.u. This arrangement is isostructural to arsenolite, As_2O_3, and senarmontite, Sb_2O_3.

2) Within the <100> array model, the <100>-LS(2×2×2) arrangement was found to be dynamically stable with an energy of 0.08 eV/f.u. This is identical to that of β-Bi_2O_3 obtained in experiments.

3) No dynamically stable arrangement for the <110> array model within the 2×2×2 supercell was found by the procedure adopted in the present study. The procedure eventually led to a structure that cannot be included in the <110> array model.

4) Two other vacancy-array models with the 2×2×2 superstructure were examined. A bixbyite-LS arrangement was found to be dynamically stable with an energy of 0.07 eV/f.u. Although no polymorph corresponding to this arrangement has been reported experimentally, it may be possible to form it under appropriate

experimental conditions. We call this phase η-Bi_2O_3.

5) Within the valentinite-array model with the 2×2×2 superstructure, the valentinite-LS arrangement was found to be dynamically stable with an energy of 0.07 eV/f.u. The vacancy array of valentinite-LS is the same as that of ε-Bi_2O_3, which was reported experimentally. Since the space group of valentinite-LS is different from that of ε-Bi_2O_3 reported experimentally, we call the phase ε'-Bi_2O_3.

6) The distribution of atom pairs in low-energy models was examined. The symmetry breaking and local distortion have a larger impact on the O sublattice than on the Bi sublattice. Both Bi-O and O-O pair distributions become evenly distributed upon lowering the symmetry, thereby lowering of energy.

7) In most previous theoretical calculations, semimetallic or metallic electronic structures were obtained for the three vacancy-array models within the single unit cell of df-Bi_2O_3. We found that a clear band gap appears in these arrangements only when the local distortion is appropriately included. There is a clear trend of the band gap decreasing with increasing relative energy.

8) β-, ε'- and η-Bi_2O_3 are suggested to be ordered low-temperature polymorphs of the disordered δ-Bi_2O_3 in the df-Bi_2O_3 family. The relative energy of β-Bi_2O_3 obtained by the present calculation agrees with the experimental transition enthalpy, ΔH, for α–β, which can be ascribed to the entropy term, $T\Delta S$, at the transition.

References

[1] N. I. Medvedeva, V. P. Zhukov, V. A. Gubanov, D. L. Novikov, and B. M. Klein, J. Phys. Chem. Solids **57,** 1243 (1996).

[2] J. M. Carlsson, B. Hellsing, H. S. Domingos, and P. D. Bristowe, Phys. Rev. B **65,** 205122 (2002).

[3] A. Walsh, G. W. Watson, D. J. Payne, R. G. Edgell, J. Guo, P. Glans, T. Learmonth, and K. E. Smith, Phys. Rev. B. **73,** 235104 (2006).

[4] D. S. Aidhy, J. C. Nico, S. B. Sinnott, E. D. Wachsman, and S. R. Phillpot, J. Am. Ceram. Soc. **91,** 2349 (2008).

[5] D. S. Aidhy, S. B. Sinnott, E. D. Wachsman, S.R. Phillpot, and J. C. Nino, J. Solid State Chem. **182,** 1222 (2009).

[6] D. S. Aidhy, S. B. Sinnott, E. D. Wachsman and S. R. Phillpot, Ionics, **16**, 297 (2010)

[7] G. Zhong, J. Wang, and Z. Zeng, Phys. Status Solidi B **245,** 2737 (2008).

[8] G. Zhong, Y. Wang, Z. Dai, J. Wang, and Z. Zeng, Phys. Status Solidi B **246,** 97 (2009).

[9] D. Music, S. Konstantinidis, and J. M. Schneider, J. Phys.: Condens. Matter **21,** 175403 (2009).

[10] C. E. Mohn, S. Stølen, S. T. Norberg, and S. Hull, Phys. Rev. Lett. **102,** 155502 (2009).

[11] C. E. Mohn, S. Stølen, S. T. Norberg, and S. Hull, Phys. Rev. B **80,** 024205 (2009).

[12] H. T. Fan, S. S. Pan, X. M. Teng, C. Ye, and G. H. Li, J. Phys. D: Appl. Phys. **39,** 1939 (2006).

[13] P. Blöchl, Phys. Rev. B **50,** 17953 (1994).

[14] G. Kresse and J. Hafner, Phys. Rev. B **47,** R558 (1993).

[15] G. Kresse and J. Furthmüller, Phys. Rev. B **54,** 11169 (1996).

[16] G. Kresse and J. Furthmüller, Comput. Mater. Sci. **6,** 15 (1996).

[17] J. P. Perdew, K. Burke, and M. Ernzerhof, Phys. Rev. Lett. **77,** 3865 (1996)

[18] A. Togo, http://fropho.sourceforge.net/.

[19] A. Togo, F. Oba, and I. Tanaka, Phys. Rev. B **77,** 184101 (2008).

[20] A. Togo, F. Oba, and I. Tanaka, Phys. Rev. B **78,** 134106 (2008).

[21] S. A. Ivanov, R. Tellgren, H. Rundlof, and V. G. Orlov, Powder Diffr. **16,** 4 (2001).

[22] T. P. Debies and J. W. Rabalais, Chem. Phys. **20,** 277 (1977).

[23] S. K. Blower and C. Greaves, Acta Crystallogr. **C44,** 587 (1988).

[24] H. A. Harwig and A. G. Gerards, Thermochim. Acta **28,** 121 (1979).

[25] C. N. R. Rao, G. V. S. Rao, and S. Ramdas, J. Phys. Chem. **73,** 672 (1969).

[26] N. Cornei, N. Tancret, F. Abraham, and O. Mentré, Inorg. Chem. Commun. **45,** 4886 (2006).

Part III

The electronic origin behind structures and energetics in M_2O_3 (M = As, Sb, Bi)

1. INTROCUCTION

As described in Part II, Bi_2O_3 have various local minimum structures and the conventional structural optimizations by first-principles calculations can lead dynamically unstable structures. Therefore, including an appropriate atomic displacement is essential for discussing structures and energetics. Similar to Bi_2O_3, sesquioxides of group 15 elements in the Periodic table, As_2O_3 and Sb_2O_3, form highly distorted structures with large open space (or low atomic density). Crystal structures of these oxides are typically far from those of simple metal oxides in which the structure can be described as a close-packed sublattice of oxide ions and cations located at either tetrahedral or octahedral interstitial sites of the sublattice. It is generally accepted that the atomic distortion can be ascribed to the presence of "lone pair" electrons, because two *n*s (n = 4, 5 and 6) electrons remain in As^{3+}, Sb^{3+} and Bi^{3+} in a formal sense. However, the relationships between their crystal structures, electronic structures and energetics have not been quantitatively investigated.

They often form several polymorphs. As_2O_3 is experimentally known to exhibit two polymorphs, i.e., cubic arsenolite and monoclinic claudetite.[1-4] Sb_2O_3 is also known to show two polymorphs, i.e., cubic α-phase (senarmontite) and orthorhombic β-phase (valentinite).[5-9] The structure of arsenolite-As_2O_3 is the same as α-Sb_2O_3. This

structure is also the same as <111>-LS arrangement of Bi_2O_3 found in Part II. β-Sb_2O_3 is isostructural to ε-Bi_2O_3.

Physical properties of crystals are generally strongly dependent on their structures. For example, Bi_2O_3 exhibits high oxide ionic conductivity in δ-phase while the other phases show very low ionic conductivity.[10] Understanding the property-structure relationships is therefore essential for selection of materials. Although these three sesquioxides have similarity in their structures, systematic studies on the structures have not been reported. In this part, energetics and crystal/electronic structures of M_2O_3 (M=As, Sb, Bi) polymorphs are systematically investigated by first-principles calculations.

Structures of these sesquioxides are seemingly quite diverse. However, a major part of them can be commonly included in a defective fluorite family which is based on a fluorite structure in which a quarter of O sites is vacant. Arsenolite-As_2O_3 and α-Sb_2O_3 are included in <111> array model. β-Sb_2O_3 and ε-Bi_2O_3 are included in valentinite-type array model. β-Bi_2O_3 is included in <100> array model. In Part II, the structures of df-Bi_2O_3 family members were investigated in detail. A series of dynamically stable structures was found by lowering symmetry along imaginary modes of lattice vibrations from the high symmetry defective fluorite structure. Experimentally reported structure of β-Bi_2O_3[11] was obtained from the <100>-HS arrangement in this way. It was also emphasized that the clear band gap of Bi_2O_3 can be found only when such a symmetry breaking is included for <100>, <110>, and <111> array models. In this report, we search dynamically stable structures of As_2O_3 and Sb_2O_3 in the same manner as those of Bi_2O_3 shown in Part II. Then the electronic origin behind their structures and energetics are discussed.

2. COMPUTATIONAL METHOD

Five array models based on the defective fluorite structure (<100>, <110>, <111>, bixbyite-type, and valentinite-type array models) were examined for the three sesquioxides. The five array models of the defective fluorite structure are shown in Fig. 11. Bixbyite- and valentinite-type array models can be made in the 2×2×2 and 1×1×2 supercell of the defective fluorite unit cell, respectively. For comparison, two different kinds of atomic arrangements within the same space group $P2_1/c$ were examined. They were taken from experimentally reported structures of claudetite-As_2O_3[12] and α-Bi_2O_3[13].

The computational details for first-principles calculations and lattice dynamics calculations are same as Part II. The first-principles calculations were performed by the PAW method[14] implemented in the VASP code.[15--17] The exchange-correlation term was treated with the Perdew-Burke-Ernzerhof (PBE) functional based on the generalized gradient approximation (GGA).[18] Plane waves were used as the basis functions with a cutoff energy of 360 eV. The convergence of the formation energy with respect to the plane-wave cutoff was found to be better than 0.01 eV/f.u. The radii of the PAW potentials were 1.11, 1.21, 1.32 and 0.98 Å for As, Sb, Bi and O, respectively. The 4*s* and 4*p* electrons for As, 5*s* and 5*p* electrons for Sb, 5*d*, 6*s* and 6*p* electrons for Bi and 2*s* and 2*p* electrons for O were treated as valence and the remaining electrons were kept frozen. At the calculation of the charge density in section 3-B and 4-A, 5*d* electrons of Bi were also kept frozen to match the number of valence electrons with As and Sb. Integration in the reciprocal space was performed by the Monkhorst-Pack scheme[19] using a 4×4×4 mesh for the <100>, <110>, <111> array model, a 4×4×2 mesh for the valentinite-type array model, a 2×2×2 mesh for the bixbyite-type array model, a 3×6×2 mesh for the claudetite-As_2O_3 model, and a 3×2×2 mesh for the α-Bi_2O_3 model. The total energy was minimized until the energy convergence became less than 1×10^{-5} eV.

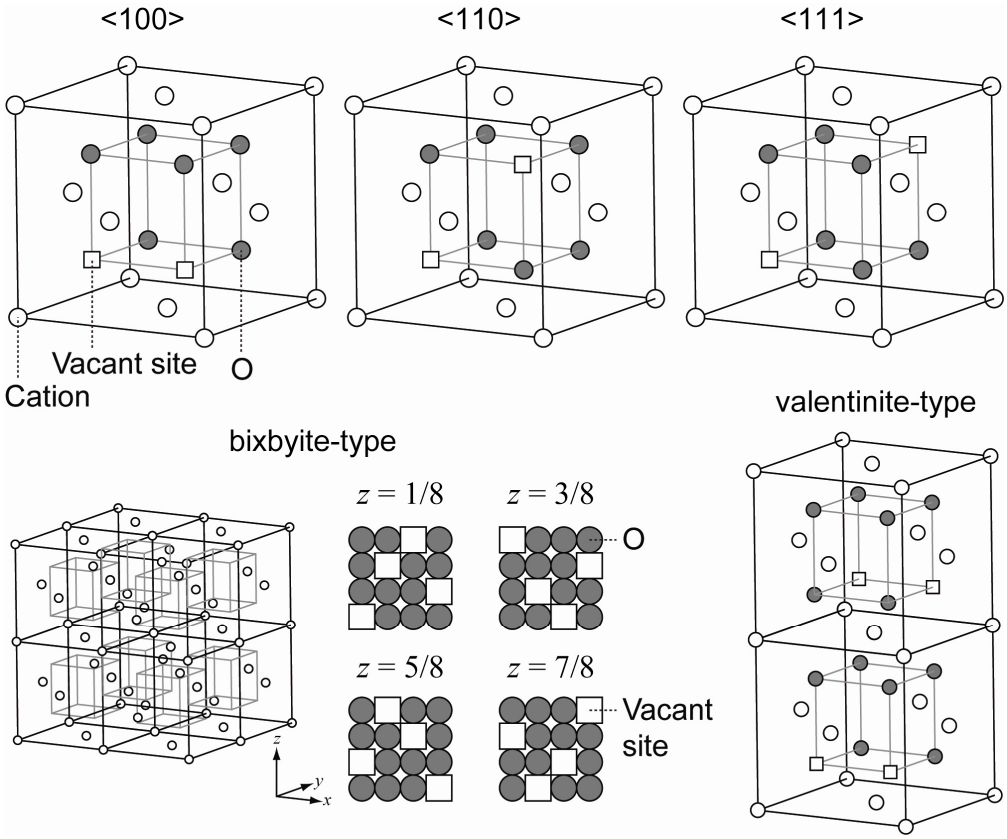

FIG. 11. The five array models of defective fluorite structure. Since the bixbyite-type array is so complicated, the array in each layer is drawn beside.

To examine the stability of the model structures against lattice dynamics, the force-constant approach involving a finite displacement was used employing the *fropho* code.[20-22] The 2×2×2 supercells of the defective fluorite structure were used with a displacement of 0.01 Å along the x, y, and z directions for each atom.

3. RESULTS

A. Symmetry breaking from ideal defective fluorite structures

Firstly all structures were optimized imposing the highest symmetry that is allowed to accommodate the array of the vacant sites in the defective fluorite structure. Then <111> and bixbyite-type array model forms cubic, <100> and <110> array model forms tetragonal, and valentinite-type array model forms orthorhombic lattice. Similar to part II, they will be hereafter called high symmetry (HS) structures. Lattice dynamics calculations were made for these defective fluorite structures. Example of phonon band structures for <111> array models of three sesquioxides are shown in Fig. 12. The imaginary value of the frequency illustrated below 0 indicates that the structure is at a local maximum of the potential surface and is unstable against the corresponding lattice vibration. All of the HS defective fluorite structures of the three sesquioxides with five different arrays show such imaginary frequencies and thus are dynamically unstable.

These HS structures were distorted by adding atomic displacement < 0.5 Å according to the vibration mode with the largest absolute value of the imaginary frequency. With this atomic displacement the symmetry were lowered. The structures were then optimized again with the new lower symmetry.

The lattice dynamics calculations were performed on the newly obtained structure. If the imaginary mode still remained, the same procedure was repeated until imaginary mode disappeared at all commensurate reciprocal lattice points of the given cell. Commensurate points correspond to the wave vectors that are commensurate with the periodicity of the examined cell. A dynamically stable structure thus obtained showing no imaginary modes at the commensurate points will be called low symmetry (LS) structure. Note that both the new arrangement and the original arrangement are

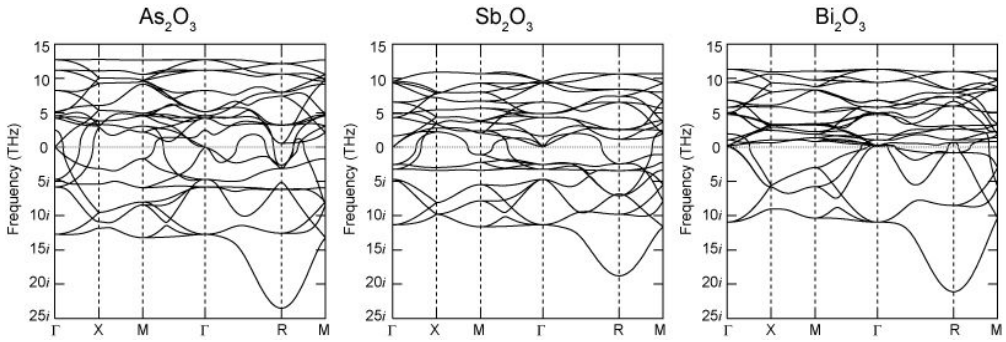

FIG. 12. Phonon band structures of the <111>-HS arrangements of the three sesquioxides.

included in the same array model. However, the symmetry is lower in the new arrangement. If the atomic displacements during the geometry optimization were too large to be described within the same oxygen atomic array models, the procedure was terminated.

The <111>-HS arrangement of As_2O_3, which is obtained by optimizing the ideal defective fluorite structure with its symmetry, shows various imaginary modes as shown in Fig. 12. The displacement along the strongest imaginary mode leads to the <111>-LS arrangement. The symmetry and atomic coordinate of the <111>-LS arrangement of As_2O_3 were found to be in good agreement with the experimentally reported structure of arsenolite-As_2O_3[1]. In the other array models, dynamically stable <100>-LS and valentinite-LS arrangements were found. Table 8 shows the four dynamically stable structural data of As_2O_3.

As for Sb_2O_3, the <111>-HS and valentinite-HS arrangements change to dynamically stable <111>-LS and valentinite-LS arrangements, respectively. They are isostructural to the experimentally reported structure of α-Sb_2O_3 and β-Sb_2O_3[5]. The structural data of the three dynamically stable arrangements are shown in Table 9.

TABLE 8. Details of calculated LS structures of As_2O_3.

	<100>-LS-As_2O_3					valentinite-LS-As_2O_3				
Space Group	$P4_2/n$ (No. 86)					$Pcc2$ (No. 27)				
Lattice Parameter	a = 7.04Å c = 8.31Å					a = 12.57Å b = 5.99Å c = 5.25Å				
Atom Coordinate	As (1)	8*g*	0.047	0.274	0.604	As (1)	4*e*	0.120	0.357	0.494
	O (1)	8*g*	0.158	0.183	0.420	As (2)	4*e*	0.380	0.143	0.420
	O (2)	4*e*	0	0.5	0.002	O(1)	2*b*	0	0.5	0.115
						O(2)	2*c*	0.5	0	0.114
						O(3)	4*e*	0.316	0.081	0.301
						O(4)	4*e*	0.184	0.581	0.301

	<111>-LS-A_2O_3					Arsenolite (experimental data[23])				
Space Group	$Fd\bar{3}m$ (No. 227)					$Fd\bar{3}m$ (No. 227)				
Lattice Parameter	a = 11.54Å					a = 11.07Å				
Atom Coordinate	As (1)	32*e*	0.774	0.774	0.774	As (1)	32*e*	0.772	0.772	0.772
	O (1)	4*e*	0.953	0.125	0.125	O (1)	4*e*	0.952	0.125	0.125

	claudetite-As_2O_3					Claudetite (experimental data[33])				
Space Group	$P2_1/c$ (No. 14)					$P2_1/c$ (No. 14)				
Lattice Parameter	a = 9.82Å b = 4.69Å c = 14.05Å β = 144.47°					a = 9.11Å b = 4.64Å c = 13.28Å β = 143.90°				
Atom Coordinate	As(1)	4*e*	0.681	0.835	0.382	As(1)	4*e*	0.685	0.831	0.383
	As(2)	4*e*	0.182	0.299	0.818	As(2)	4*e*	0.188	0.292	0.816
	O (1)	4*e*	0.608	0.460	0.322	O (1)	4*e*	0.614	0.459	0.333
	O (2)	4*e*	0.955	0.149	0.769	O (2)	4*e*	0.946	0.140	0.762
	O (3)	4*e*	0.394	0.358	0.033	O (3)	4*e*	0.401	0.349	0.034

TABLE 9. Details of calculated LS structure of Sb_2O_3.

	<111>-LS-Sb_2O_3					α-Sb_2O_3 (experimental data[6])				
Space Group	$Fd\bar{3}m$					$Fd\bar{3}m$				
Lattice Parameter	a = 11.42Å					a = 11.15Å				
Atom Coordinate	Sb (1)	32*e*	0.887	0.887	0.887	Sb (1)	32*e*	0.885	0.885	0.885
	O (1)	4*e*	0.186	0	0	O (1)	4*e*	0.186	0	0

	valentinite-LS-Sb_2O_3					β-Sb_2O_3 (experimental data[6])				
Space Group	*Pccn* (No. 56)					*Pccn* (No. 56)				
Lattice Parameter	a = 5.20Å b = 12.56Å c = 5.52Å					a = 4.91Å b = 12.46Å c = 5.41Å				
Atom Coordinate	Sb (1)	8*e*	0.053	0.127	0.180	Sb (1)	8*e*	0.041	0.127	0.178
	O (1)	8*e*	0.25	0.25	0.018	O (1)	8*e*	0.25	0.25	0.023
	O(2)	4*c*	0.151	0.057	0.857	O(2)	4*c*	0.152	0.059	0.855

	claudetite-Sb_2O_3				
Space Group	$P2_1/c$ (No. 14)				
Lattice Parameter	a = 9.73Å b = 4.87Å c = 14.51Å β = 146.56°				
Atom Coordinate	Sb (1)	4*e*	0.710	0.855	0.408
	Sb (2)	4*e*	0.207	0.330	0.809
	O (1)	4*e*	0.621	0.462	0.336
	O (2)	4*e*	0.988	0.176	0.795
	O (3)	4*e*	0.443	0.400	0.049

Besides the sets of defective fluorite structures, two different kinds of monoclinic structures with the space group of $P2_1/c$ were examined. The energy of the claudetite-As_2O_3 type arrangement is lower than α-Bi_2O_3 type arrangement by 0.23 eV/f.u. in As_2O_3 and 0.12 eV/f.u. in Sb_2O_3. On the other hand, α-Bi_2O_3 type arrangement is more stable than claudetite-As_2O_3 type arrangement by 0.13 eV/f.u. in Bi_2O_3. Energetically lower structure will be hereafter referred to as the $P2_1/c$ model of each sesquioxide. These $P2_1/c$ models are found to be dynamically stable. The relative energies of each arrangement against the $P2_1/c$ models are summarized in Fig. 13. The open marks correspond to the dynamically unstable arrangements, and the solid marks correspond to the dynamically stable LS arrangements.

In As_2O_3, four of dynamically stable structures exhibit relative energies of < 0.1eV/f.u. Among them claudetite-As_2O_3 type arrangement has the lowest energy. Although arsenolite-As_2O_3 is the low temperature phase in the experimental report, the corresponding arrangement, <111>-LS arrangement, shows 0.05 eV/f.u. higher energy than that of the claudetite-As_2O_3 type arrangement. The variation of relative energies in Sb_2O_3 within three of dynamically stable structures is also < 0.1eV/f.u. Similarly to As_2O_3, the energetical hierarchy between α-Sb_2O_3 and β-Sb_2O_3 by the present calculations does not well agree with that by experiments. The relative energy of the low temperature phase α-Sb_2O_3 which corresponds to <111>-LS arrangement is 0.06 eV/f.u. higher than the high temperature phase β-Sb_2O_3 which corresponds to valentinite-LS arrangement. The origin of the inconsistency in the energetical hierarchy is not clear at the moment. This may be related to the choice of exchange and correlation functionals in the DFT calculations. As a matter of fact, the relative energy of the α-Sb_2O_3 became 0.004 eV/f.u. lower than β-Sb_2O_3 when we use hybrid

functional of HSE for otherwise in the same calculation. More detailed study is required in the future to discuss the energetics among polymorphs with the order of < 0.1 eV/f.u., which is beyond the scope of the present study.

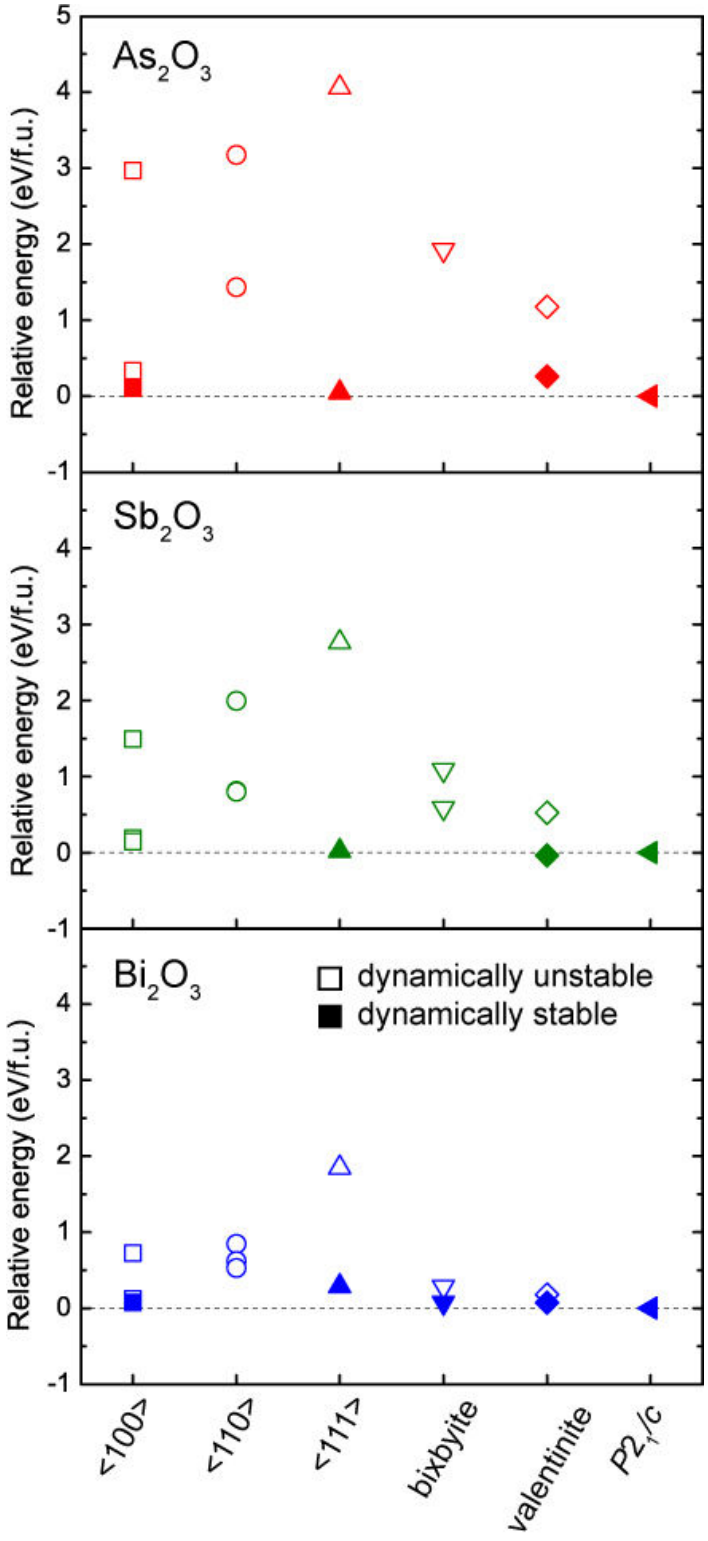

FIG. 13. The relative energies of each arrangement against the monoclinic $P2_1/c$ structure.

B. Local atomic arrangements of dynamically stable structures

As described in the previous section, the energy of each array model is lowered considerably with symmetry breaking and local atomic distortion. In this section, the local atomic arrangements of the stable structures are investigated.

Among the five array models based on defective fluorite structure, the <111>-LS arrangements of the three sesquioxides have the same space group. The <111>-HS arrangement has $Pn\bar{3}m$ space group with 10 atoms unit cell. It transforms to <111>-LS arrangement which has $Fd\bar{3}m$ space group with 80 atoms unit cell in the three sesquioxide. We therefore compare HS and LS arrangements of the three sesquioxides with <111> array model in detail. Both HS and LS arrangements have one cation site and one O site. The cation is coordinated by six O ions and twelve cations. Figure 14 shows the projection of the <111>-HS and LS arrangements of As_2O_3 from [110] direction. As can be clearly seen in Fig. 14, ions tend to aggregate in the LS arrangement, while they are evenly distributed in the HS arrangement. Similar trends

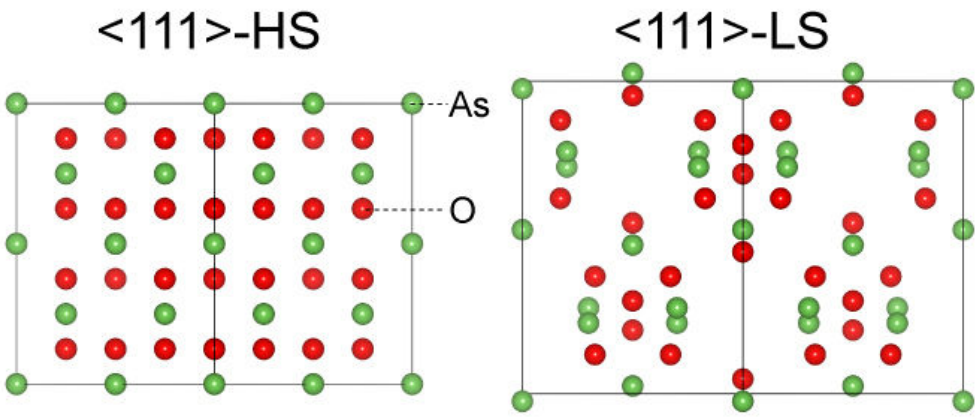

FIG. 14. The projection of the <111>-HS and LS arrangements of As_2O_3 from [110] direction

can be seen in Sb_2O_3 and Bi_2O_3. Figure 15 shows the interatomic distances between (a) cation-O and (b) cation-cation in the <111>-HS and -LS arrangements of three sesquioxides. The numbers beside the bars are the degeneracy. All the interatomic distance between cation-O and cation-cation are the same in the HS arrangement. However in the LS arrangement a part of them are shortened and the others are elongated by the local distortion. With the local distortion, the atomic density locally decreases in the <111>-LS arrangement. We can anticipate that the valence electron density also locally decreases with the local distortion. In order to confirm the idea, the spatial distribution of the valence electron density is analyzed. Distribution of the valence electron density in the 80 atoms cells are compared in Fig. 16. The charge density within the core radius of the PAW potentials was excluded from the calculation of the valence electron density. Black solid line and colored bar graph correspond to the <111>-HS and LS arrangements, respectively. In the HS arrangement, each profile shows a peak at around 0.05 $Å^{-3}$. On the other hand, the peak shifts towards lower valence electron density in the LS arrangement. This implies that the volume fraction of the low valence electron density significantly increases in the LS arrangement. The change of the electron density is largest for As_2O_3 and smallest for Bi_2O_3. This can be mainly ascribed to the volume expansion associated with the transformation. Table 10 shows the lattice constant of the cubic structure and volume expansion of 80 atoms cell of the <111>-HS and LS arrangements of three sesquioxides. The volume increases by 47% in As_2O_3, whereas it is only 6% in Bi_2O_3.

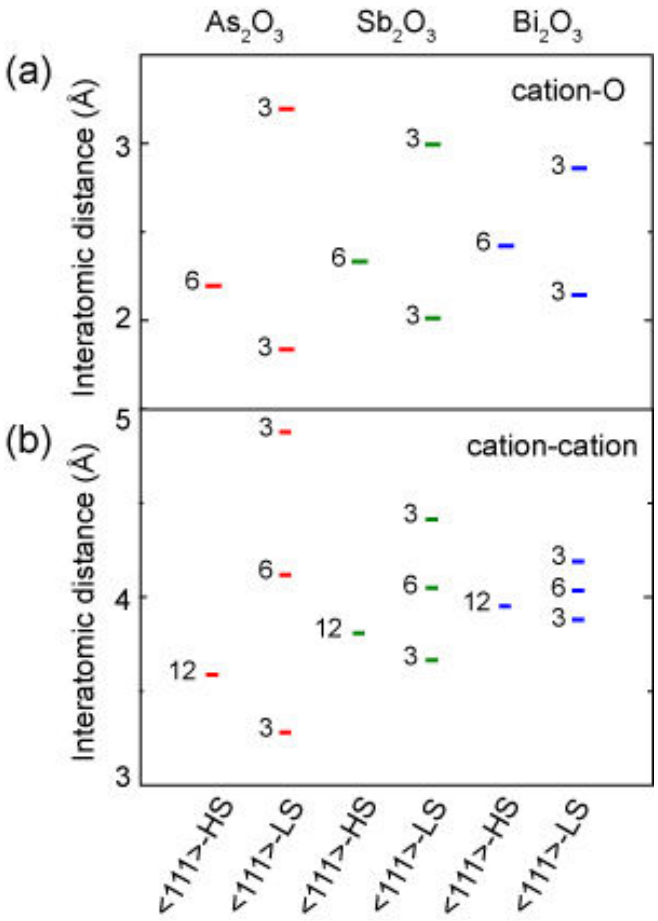

FIG. 15. The interatomic distance between (a) cation-O and (b) cation-cation in the <111>-HS and -LS arrangements of three sesquioxides.

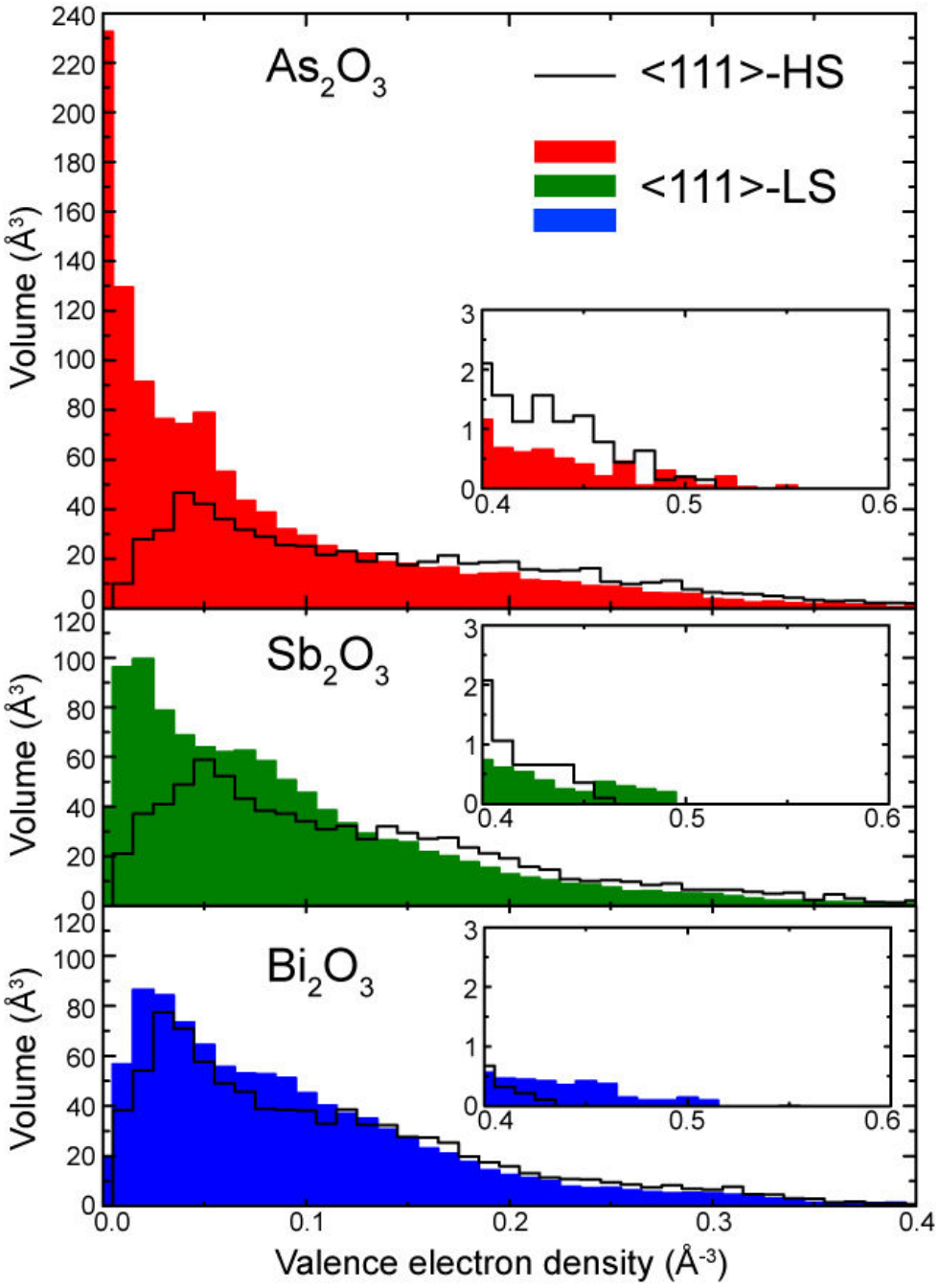

FIG. 16. The distribution of valence electron density in the <111>-HS and LS arrangements of the three sesquioxides. The parts of larger valence electron density are shown in insets.

TABLE 10. The lattice constant and volume expansion of 80 atoms cell in the <111>-HS and LS arrangements of three sesquioxides.

	<111>-HS	<111>-LS	Volume expansion
As_2O_3	10.13Å	11.54Å	47%
Sb_2O_3	10.77Å	11.42Å	19%
Bi_2O_3	11.18Å	11.41Å	6%

C. Electronic structures of dynamically stable structures

Sb_2O_3 was reported to have a clear band gap by expeiments.[23-25] As_2O_3 was also reported to have a optical band gap by calculation using experimental parameter.[26] However, the HS structures of 10 atoms unit cell, <100>-HS, <110>-HS and <111>-HS arrangements, for the three sesquioxides have either metallic or semimetallic electronic structure in which an energy band cross the Fermi level or the top of the valence band had a higher energy than the bottom of the conduction band. These differences from the experimental report are similar to Bi_2O_3 as described in Part II. When the symmetry breaking and local distortion are included into these structures, the band gap appears. All of LS arrangements for the three sesquioxides have clear band gap. They are summarized in Table 11. Since we are not able to obtain the LS arrangement in some array models, some values are missing. α-Sb_2O_3 and β-Sb_2O_3 were reported to have the band gap of 4 eV[22-24] and 3.3 eV[22], respectively. The corresponding theoretical values in this work are 3.50 eV (<111>-LS) and 2.66 eV (valentinite-LS), respectively. The underestimation may be ascribed to the use of GGA for the exchange and correlation functionals. As a matter of fact, the band gaps calculated with the hybrid functional of

TABLE 11. The calculated band gap of each LS structures. The unit is eV.

	<100>-LS	<111>-LS	bixbyite-LS	valentinite-LS	$P2_1/c$
As_2O_3	3.79	4.13		3.23	3.70
Sb_2O_3		3.5		2.66	2.60
Bi_2O_3	2.11	2.66	2.66	2.52	2.25

HSE for otherwise in the same calculation are 4.28 eV (<111>-LS) and 3.60 eV (valentinite-LS), respectively. They are much closer to the experimental results.

Figure 17 and 18 shows the relation between the relative energy and band gap for each array model of As_2O_3 and Sb_2O_3. Similar to Bi_2O_3, there is a trend that the band gap decreases with the increase of the relative energy among different arrangements. The local distortion affects the electronic structure significantly. Inclusion of the symmetry breaking and the local distortion is therefore essential to properly describe the energetics and electronic structures of three sesquioxides.

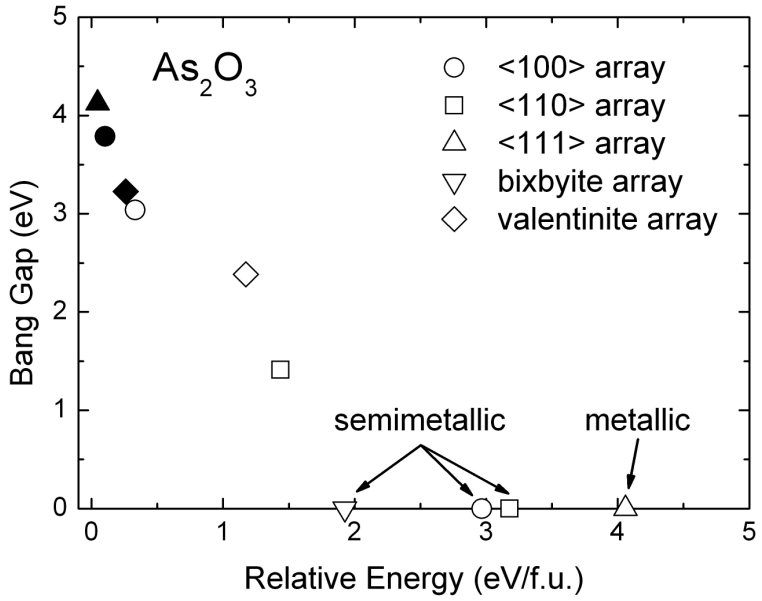

FIG. 17 Relation between band gap and relative energy for each array model of As_2O_3. Array models are distinguished by the shape of marks. The open marks correspond to the dynamically unstable arrangements, and the solid marks correspond to the dynamically stable LS arrangements.

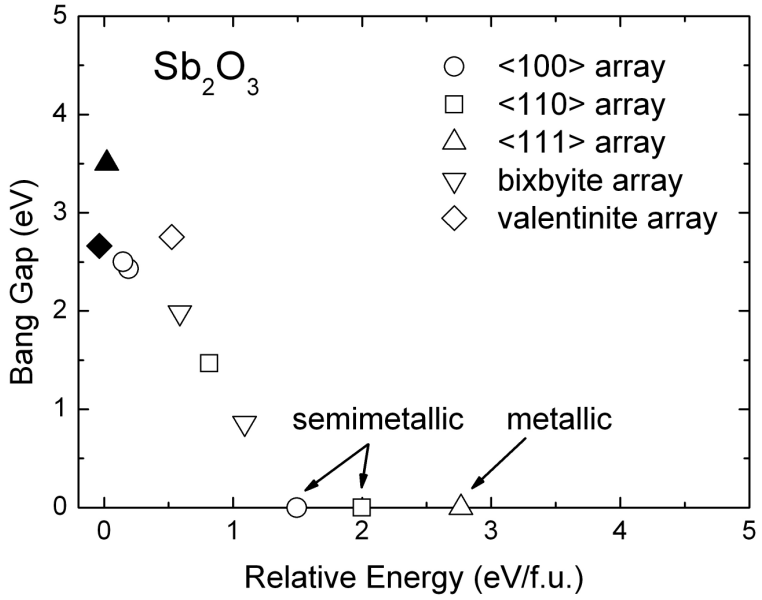

FIG. 18 Relation between band gap and relative energy for each array model of Sb_2O_3.

4. DISCUSSION

A. Electronic localization

In sesquioxide of late group 15 elements, two *n*s-electrons remain in the valence band in a formal sense. When they are localized to the cations and form asymmetric charge distribution, they are referred to as “lone pair”. The lone pair often play a central role for the local atomic distortion. In order to examine the origin of the local atomic distortion and the symmetry breaking, we examine the charge distribution of the sesquioxides in detail.

Figure 19 shows the isosurface of valence electron density distribution around the cation in the <111>-HS and LS arrangements of the three sesquioxides. Atomic arrangements can be easily understood in the HS arrangement. The cation is coordinated by six O ions and two empty sites. The empty sites are located at the left-bottom-front and right-top-back in the cubic structure shown in Fig. 19(a). With the HS to LS transformation, O ions move toward the empty site at the left-bottom-front as can be seen in Fig. 19(b). Then the other empty site at the right-top-back shares larger open space as compared to the corresponding space in the HS arrangement. In the HS arrangement, electrons spherically distribute around the cation, as shown in Fig. 19(a). The isosurface of 0.6 $Å^{-3}$ for As2O3, 0.4 $Å^{-3}$ for Sb_2O_3 and 0.3 $Å^{-3}$ for Bi_2O_3 cannot be seen around the cation. On the other hand, as shown in Fig. 19(b), the charge density around the cation became asymmetric and more localized in the LS arrangements and distribute along the direction of the empty site at the right-top-back.

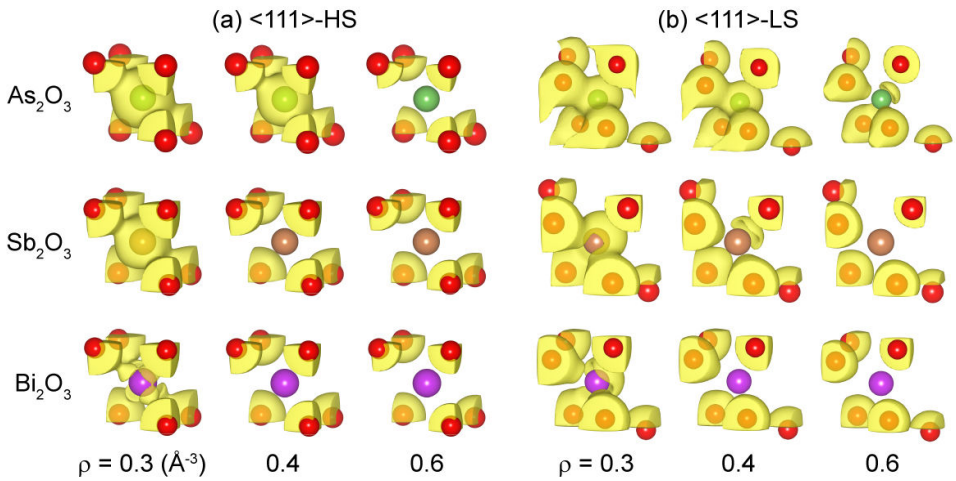

FIG. 19. The isosurface of the valence electron density distribution around the cation in the (a) <111>-HS and (b) LS arrangements of the three sesquioxides. A part of the unit cell is extracted. Red spheres are oxygen ions. Green, brown, and violet spheres are cations.

To inspect the formation of the lone pair in more detail, partial charge-density distribution is investigated. Figure 20 shows the electron density of states in the <111>-LS arrangement of As_2O_3. The top of valence band is set to be zero. The valence band is mainly composed of O 2*p* state with minor contributions of As 4*s* and 4*p*. The valence band is divided into four regions, i.e., (a) -6.5 to -4.8 eV, (b) -4.8 to -1.9 eV, (c) -1.9 to -0.9 eV, and (d) -0.9 to 0 eV. On the basis of quantum chemistry intuition, O 2*p* and As 4*sp* form bonding interaction in the region (a) and anti-bonding in the region (d). The isosurface of partial valence electron density distribution of each region is shown in Fig. 21. The electrons belong to the region (d) shows the isosurface elongated toward the direction of the empty site. This indicates that the As 4*s* and 4*p* electrons in the energy region (d) contribute significantly to the anisotropic and localized charge distribution. In other words, "lone pair" is formed, which plays an important role for the local atomic distortion and the symmetry breaking. Similar lone pair can be seen in the <111>-LS arrangement of Sb_2O_3 and Bi_2O_3 (Fig. 19(b)).

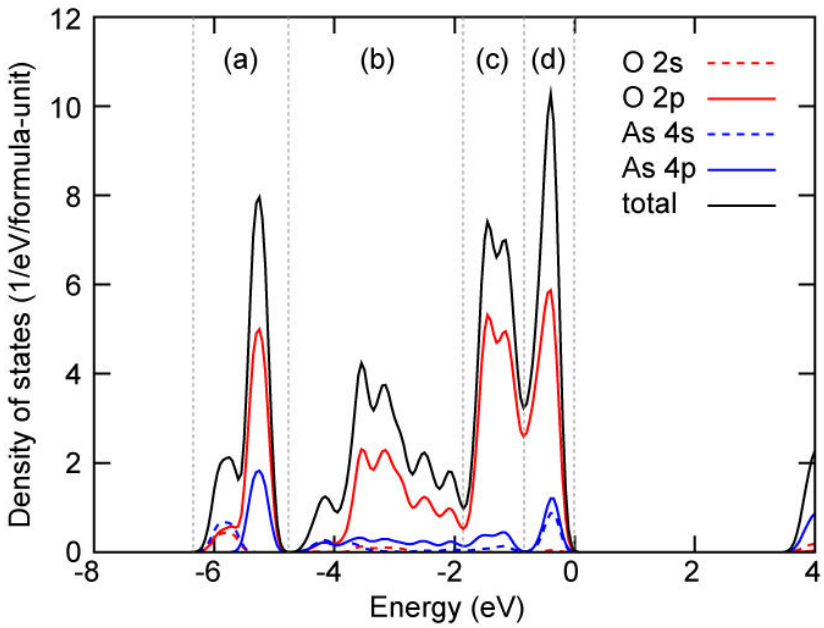

FIG. 20. The partial electron density of states of <111>-LS arrangement of As_2O_3. The top of valence band is set to 0. Black line represents the total density of states. Red dotted and solid lines represent O 2s state and O 2p state, respectively. Blue dotted and solid lines represent As 4s state and As 4p state, respectively.

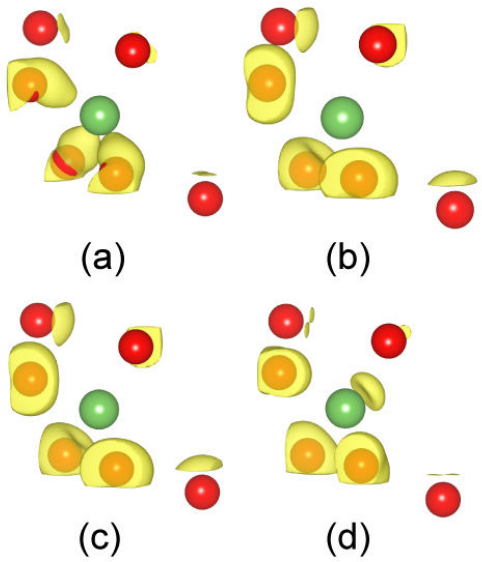

FIG. 21. The isosurface of valence electron density distribution of each region (See Fig. 20) around cation in <111>-LS arrangement of As_2O_3. The isosurface of 0.2 $Å^{-3}$ is shown. Green and red spheres represent As and O ions, respectively.

B. Electronic mechanism behind the formation of the LS arrangements

The dominant term of the formation energy of an ionic compound should be the electrostatic energy that can be correlated to the Madelung energy as computed with formal charges of constituent ions. In the present sesquioxides, however, local atomic distortion may not be driven by the simple electrostatic energy. In order to discuss the contributions to the formation energy, the Madelung energies of all structures are computed with the formal ionic charges of +3 for cations and -2 for oxygen using the GULP code.[27] Figure 22 shows the relationship between the DFT relative formation energy and the relative Madelung energy. The energy of the $P2_1/c$ model in each oxide is set to be zero. Open and solid marks denote dynamically unstable and stable arrangements, respectively. Array models are distinguished by the shape of marks.

Dotted lines in the figure has a slope of unity. The relative DFT energy can be ascribed to the relative Madelung energy when data points are on the dotted line. In As_2O_3, many of data points for dynamically unstable structures are located close to the line, roughly speaking. On the other hands, the DFT energies of four dynamically stable structures are found to be independent of the Madelung energy. In other words, the contribution of the electrostatic energy as expressed by the Madelung term is minimal to the DFT formation energies in the dynamically stable structures. The other contributions such as formation of covalent bondings and formation of lone pair should be dominant for lowering of the DFT formation energy in dynamically stable structures. The energy gain associated with the formation of the dynamically stable LS structures from the HS structures is the order of 1 eV/f.u., which is important for determining the crystal structures with large atomic distortion. The contribution of the electrostatic energy is also very small to the DFT formation energies in the dynamically stable structures of Sb_2O_3 and Bi_2O_3. It can be concluded that the formation of largely distorted structures

in these three sesquioxdes cannot be explained by the simple electrostatic picture. Detailed analysis of the electronic structures associated with the formation of lone pair is therefore essential.

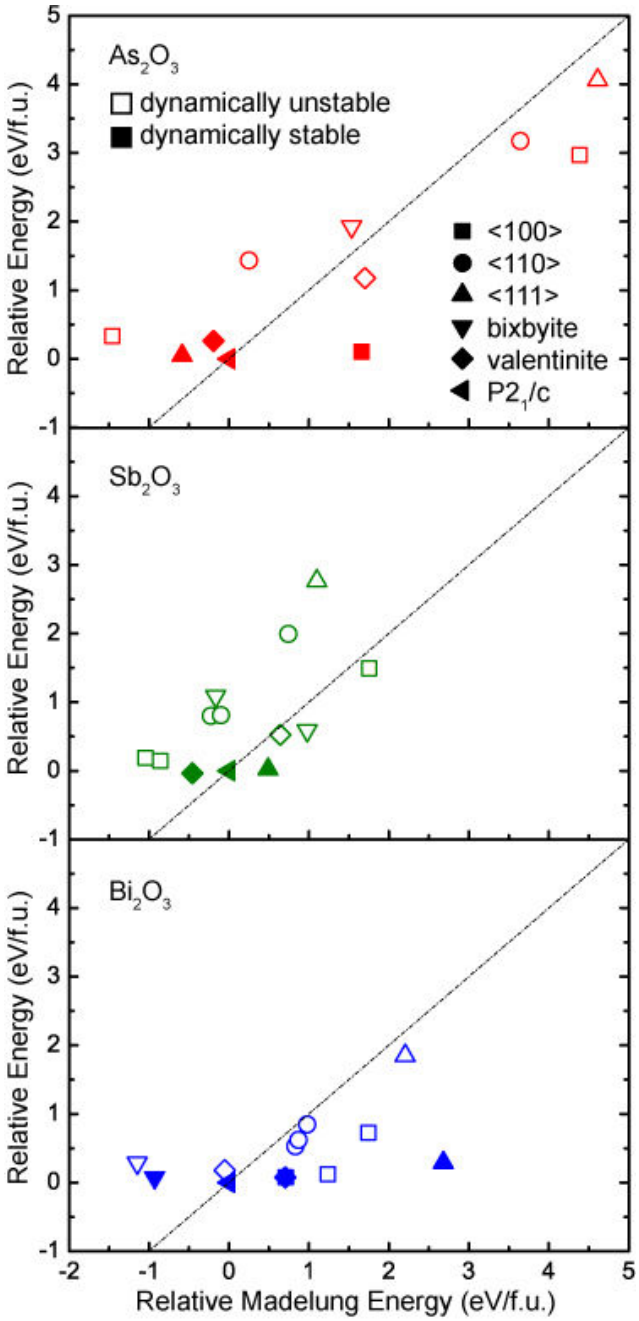

FIG. 22. The calculated energy against Madelung energy. Each value is the relative value against the energy of the $P2_1/c$ model.

5. Summary

First-principles lattice-dynamics calculations were systematically made for M_2O_3 (M=As, Sb, Bi). Dynamically stable LS structures were searched by including atomic displacements along imaginary modes of lattice vibrations that appear in HS defective fluorite structures. Atomic arrangements, electronic structures and energetics of the LS structures were then examined in detail. Major results in this study can be summarized as follows:

1) All of five array models with the HS defective fluorite arrangements were dynamically unstable against various vibration modes. When the symmetry breaking and local distortion were included, some LS structures became dynamically stable. The majority of the experimentally reported structures (arsenolite-As_2O_3, α-Sb_2O_3, β-Sb_2O_3 and β-Bi_2O_3) were obtained in this procedure. At the same time, some dynamically stable structures as yet-unknown by experiments were discovered. Formation energy of these dynamically stable structures were smaller than 0.1eV/f.u., relative to $P2_1/c$ models with claudetite-As_2O_3 type arrangement for M=As and Sb, and with α-Bi_2O_3 type arrangement for M=Bi (Fig. 13).

2) Ions tend to aggregate in the LS arrangement, while they were evenly distributed in the HS arrangement (Fig. 14). All of interatomic distances between cation-anion and cation-cation were the same in the HS arrangement. However in the LS arrangement a part of them were shortened and the others were elongated by the local distortion (Fig. 15). The valence electron density locally decreased with the local distortion associated with the HS-LS transformation (Fig. 16).

3) Although the HS arrangements for three sesquioxides showed either metallic

or semimetallic electronic structure, all of LS arrangements exhibited clear band gaps (Table 11), which is in good agreements to experimental reports. Inclusion of the symmetry breaking and the local distortion is therefore essential to properly describe the energetics and electronic structures of three sesquioxides.

4) In the HS arrangement, electrons spherically distributed around the cation. On the other hand in the LS arrangements, the charge density around the cation became asymmetric and distributed along the direction of the empty site (Fig. 19). The As 4*s* and 4*p* electrons near the top of the valence band (region (d) in Fig. 20) contributed significantly to the anisotropic and localized charge distribution (Fig. 21), i.e., the formation of lone pair. This played an important role for the local atomic distortion and the symmetry breaking.

5) The energy gain associated with the formation of the largely distorted LS structures from the HS structures was the order of 1 eV/f.u., which cannot be explained by the simple electrostatic picture (Fig. 22). Detailed analysis of the electronic structures by taking account the symmetry breaking, local distortion and the formation of lone pair were therefore essential for discussing the relation between structures, stability and properties in these sesquioxides.

References

[1] F. Pertlik, Czech. J. Phys. B **28**, 170 (1978).

[2] A. J. Frueh, Am. Minerologist **36**, 833 (1951).

[3] F. Pertlik, Monatsh. Chem. **109**, 277 (1978).

[4] D. Ležal, K. Koňak, J. Non-Cryst. Solids **192&193**, 187 (1995).

[5] C. Svensson, Acta. Crystallogr. Sect. B **30**, 458 (1974).

[6] C. Svensson, Acta. Crystallogr. Sect. B **31**, 2016 (1975).

[7] S. J. Gilliam, J. O. Jensen, A. Banerjee, D. Zeroka, S. J. Kirkby, and C. N. Merrowa, Spectrochim. Acta Part A **60**, 425 (2004).

[8] R. G. Orman, D. Holland, J. Solid State Chem. **180**, 2587 (2007).

[9] E. I. Voit, A. E. Panasenko, and L. A. Zemnukhova, J. Struct. Chem. **50**, 60 (2009)

[10] T. Takahashi, H. Iwahara, and Y. Nagai, J. Appl. Electrochem. **2**, 97 (1972).

[11] S. K. Blower and C. Greaves, Acta Crystallogr. **C44**, 587 (1988).

[12] F. Pertlik, Monatsh. Chem. **106**, 755 (1975)

[13] H. A. Harwig, Z. Anorg. Allgem. Chem., **444**, 151 (1978).

[14] P. Blöchl, Phys. Rev. B **50**, 17953 (1994).

[15] G. Kresse and J. Hafner, Phys. Rev. B **47**, R558 (1993).

[16] G. Kresse and J. Furthmüller, Phys. Rev. B **54**, 11169 (1996).

[17] G. Kresse and J. Furthmüller, Comput. Mater. Sci. **6**, 15 (1996).

[18] J. P. Perdew, K. Burke, and M. Ernzerhof, Phys. Rev. Lett. **77**, 3865 (1996).

[19] H. J. Monkhorst and J. D. Pack, Phys. Rev. B **13,** 5188 (1976)

[20] A. Togo, http://fropho.sourceforge.net/.

[21] A. Togo, F. Oba, and I. Tanaka, Phys. Rev. B **77**, 184101 (2008).

[22] A. Togo, F. Oba, and I. Tanaka, Phys. Rev. B **78**, 134106 (2008).

[23] C. Wood and B. V. Pelt, A. Dwight, Phys. Status Solidi B **54**, 701 (1972)

[24] N. Tigau, V. Ciupina, and G. Pradan, J. Cryst. Growth **277**, 529 (2005)

[25] N. Tigau, V. Ciupina, and G. Prodan, J. Optoelectron. Adv. Matter. **8**, 37 (2006)

[26] J. Portier, G. Campet, C. W. Kwon, J. Etourneau, M. A. Subramanian, Int. J. Inorg. Mater. **3,** 1091 (2001)

[27] J. D. Gale, J. Chem. Soc., Faraday Trans. **93,** 629 (1997)

Part IV
First principles molecular dynamics calculations on defective fluorite Bi_2O_3

1. INTRODUCTION

In the molecular dynamics (MD) method the position of the atom at each time is calculated based on the Newton equation. The classical MD calculations use an empirical potential to calculate the force. The parameter of potential is determined by experimental or calculational result. Since the calculational cost of classical MD calculations is small, a large system or long time period is possible to be simulated. However, the reliability of the calculation depends significantly on the appropriacy of the used potential. On the other hand, in the first-principles MD calculations, the force is calculated by first-principles calculation. The reliability of the calculations is therefore preserved within the accuracy of the first-principles calculations. However, the calculational cost is so high and applicable system is limited. Since MD method can consider an effect of fluctuation, this method is thought to be suitable for high ionic conductor including Bi_2O_3 to see the movement of ions. For example, the diffusion of O ions in ZrO_2 is widely investigated.[1-3]

MD method has also been performed on Bi_2O_3 to get the information of the local structure or the diffusion of O ions. Jacobs and Macdonaill calculated Bi-Bi and O-O potentials by experiment and Bi-O potential by calculation.[4] They indicated that the oxygen interstitials on 48*i* sites with their calculated potentials. Aidhy et al. used the same potential which Jacobs calculated and found a low energy arrangement of vacant sites.[5] They also showed the importance of atomic polarizability for oxygen diffusion.[6]

Mohn et al. performed the first-principles MD calculations.[7] They investigated the pair distribution and angular distribution functions of δ- and β-Bi_2O_3. The self-diffusion coefficient in δ-Bi_2O_3 was also estimated.

In Part II, it was suggested that β, η, and ε' phase are ordered low-temperature phase of the disordered δ-Bi_2O_3 in the df-Bi_2O_3 family. Assuming that, it can be speculated that the array of the oxygen sublattice in these structures gets disordered at an order-disorder transition temperature. However, the past reports on Bi_2O_3 using MD method have not investigated such an order-disorder transition or focused on the relation between O ionic diffusion and initial structure. In this part, we discuss the movement of O ions in the three stable structures, β, η and ε' phase, at various temperatures by first-principles MD calculations.

2. COMPUTATIONAL METHOD

The first-principles MD calculations were performed using VASP code[8-10] which is based on the PAW method.[11] The initial structures were constructed according to the <100>-LS, bixbyite-LS and valentinite-LS arrangement found in Part II. Firstly, each structure was transformed to 80 atoms cubic cell and the atomic coordinate was optimized within the cubic cell. The lattice constant was set as 11.4 Å, which was taken from the lattice constant of bixbyite-LS arrangement. The shape of cell was fixed during the MD calculation. We call hereafter these cubic models cubic-β (c-β), cubic-η (c-η) and cubic-ε' (c-ε') phase, respectively. The simulations were done for three times at each temperature of every 100 K from 700 to 1200 K. The temperature was controlled by a Nosé thermostat, which creates a canonical (NVT) ensemble. The time step was set as 2 fs and each simulation was done by 15000 MD steps (30 ps) in total.

Plane waves up to an energy cutoff of 360 eV and 300 eV were used as basis functions for structural optimization and MD calculations, respectively. Bi 6*s*, 6*p* and O 2*s*, 2*p* electrons were treated as the valence state. We also examined the MD calculations with higher cutoff energy or including Bi 5*d* electrons as valence. However, the results are not so different for the following discussion. The exchange-correlation term was treated with the Perdew-Burke-Ernzerhof (PBE) functional based on the generalized gradient approximation (GGA)[12]. Integration in the reciprocal space was performed only at Γ point for MD calculations and the Monkhorst-Pack scheme using a 2×2×2 mesh for structural optimization of the 80 atoms cell.

3. RESULTS

A. Diffusion of oxygen ions

As described in Part II, the energy difference between <100>-LS, bixbyite-LS and valentinite-LS arrangement is less than 0.01 eV/f.u. However, the energies of <100>-LS and valentinite-LS arrangement are raised by the transformation to cubic cell. As a result of atomic coordinate optimization, the energy of c-η is the lowest and that of c-β and c-ε is 0.01 eV/f.u. higher than c-η. Starting with these structures, the diffusion of O ions at each temperature is investigated. Figure 23-28 shows the mean square displacement (MSD) of O ions. MSD is the average of the square of displacement from the initial position, which is given by

$$\mathrm{MSD} = \frac{1}{N}\sum_{i}\left(\boldsymbol{r}_i(t) - \boldsymbol{r}_i(0)\right)^2$$

where N is the number of O ions and 48 at this time. $\boldsymbol{r}_i(t)$ is the position of ion i at time t. Each ion does not have kinetic energy at time 0. They get energy from thermostat to be the given temperature. Therefore the first period in MD calculation is so different from the equilibrium state that the temperature fluctuate more than 1000 K. Thus ions can have too large kinetic energy and large jump of MSD can be seen at the first period in some simulations. Since it takes some MD steps to make the fluctuation of temperature valid, the calculation of MSD is started after 400 MD steps (0.8 ps). Note that the first period in the graphs is still considered as not equilibrium state. Blue, red and green lines in the graphs correspond to the c-β, c-η and c-ε', respectively. Since we did three simulations for each phase at each temperature, there are nine lines in the graph. At 700 K, O ions hardly move and the MSD is almost 0 for all phase as shown in Fig 23. However, the MSD gradually increase with the time in Fig24. As the temperature increase more, the slopes of the lines also increase as shown in Fig. 25-28. In these

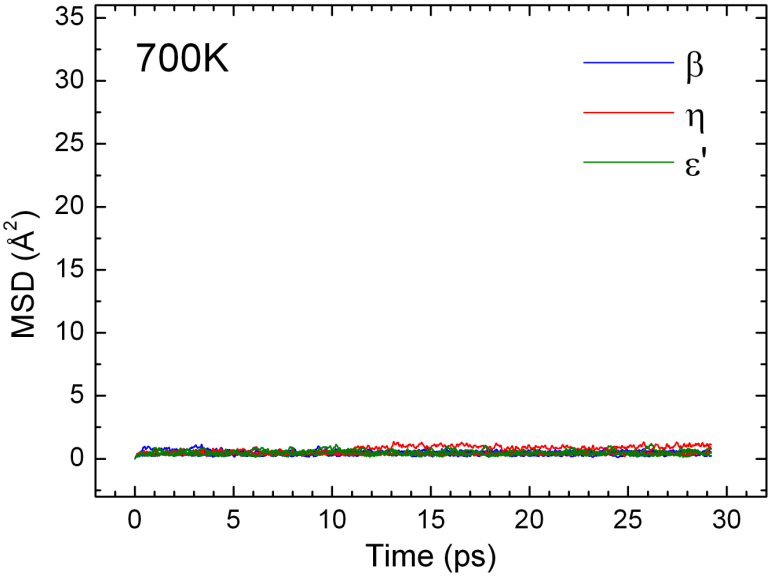

FIG. 23. The mean square displacement of O ions at 700 K. Blue, red and green lines correspond to c-β, c-η and c-ε', respectively.

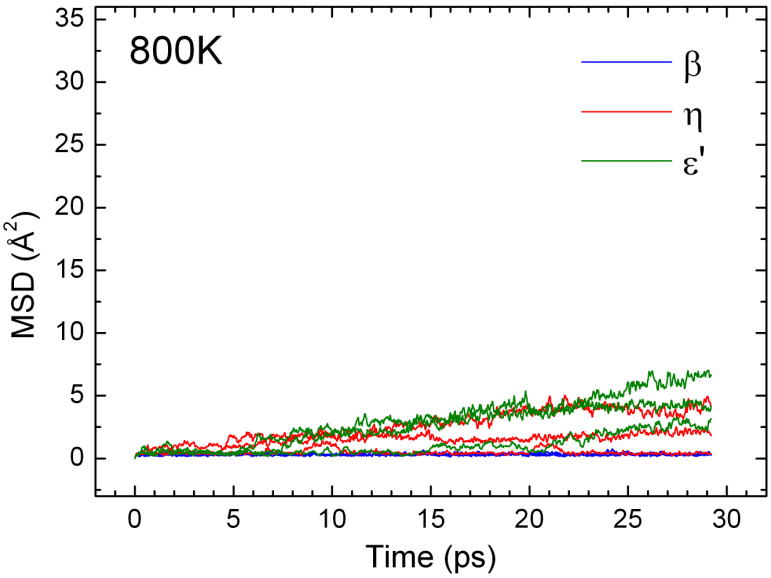

FIG. 24. The mean square displacement of O ions at 800 K. Blue, red and green lines correspond to c-β, c-η and c-ε', respectively.

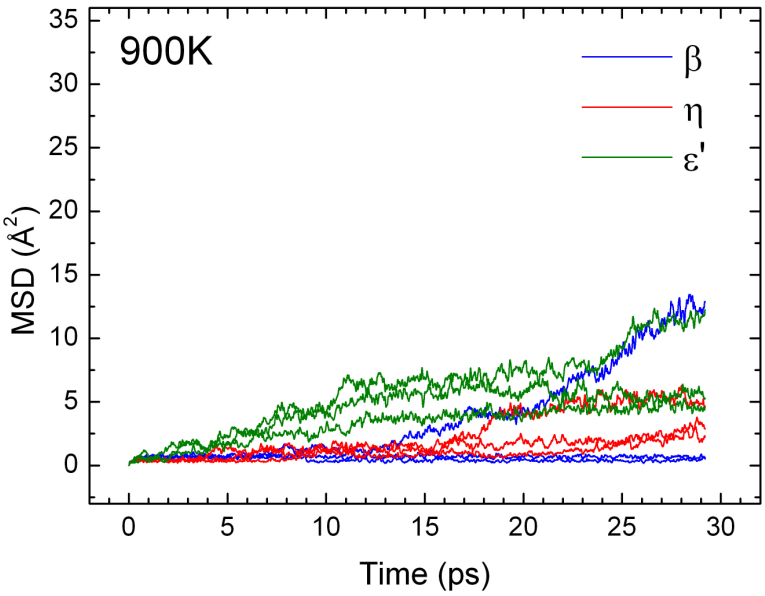

FIG. 25. The mean square displacement of O ions at 900 K. Blue, red and green lines correspond to c-β, c-η and c-ε', respectively.

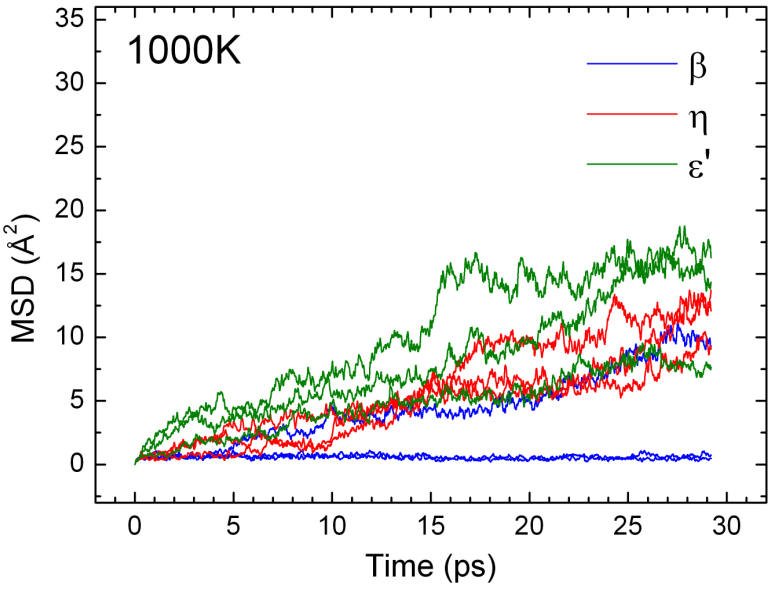

FIG. 26. The mean square displacement of O ions at 1000 K. Blue, red and green lines correspond to c-β, c-η and c-ε', respectively.

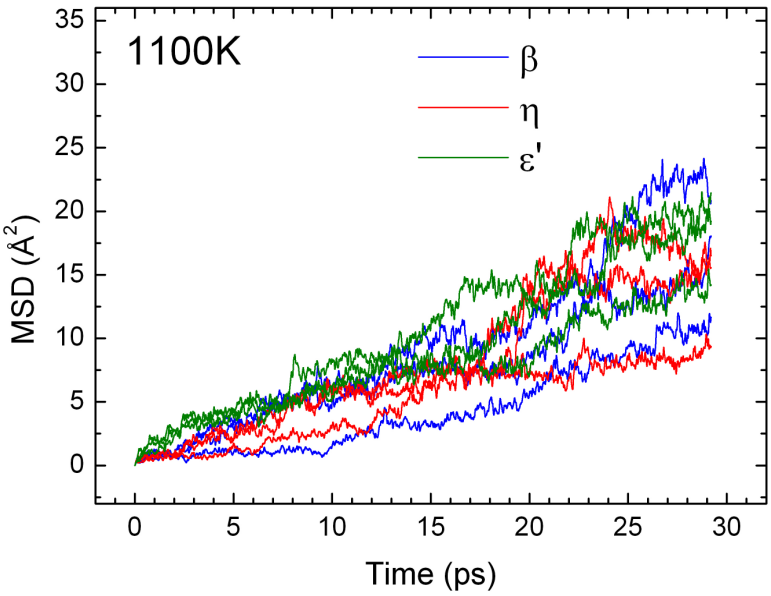

FIG. 27. The mean square displacement of O ions at 1100 K. Blue, red and green lines correspond to c-β, c-η and c-ε', respectively.

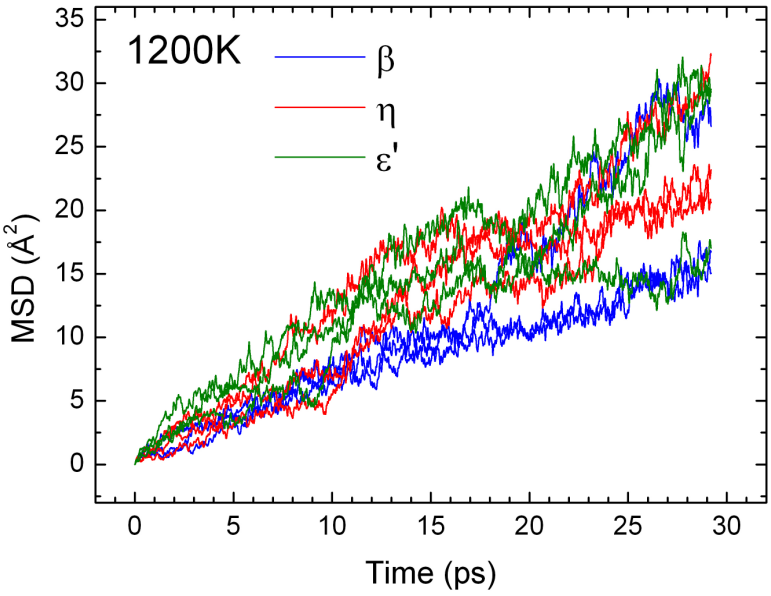

FIG. 28. The mean square displacement of O ions at 1200 K. Blue, red and green lines correspond to c-β, c-η and c-ε', respectively.

graphs, the MSD have considerable difference even between the same phases. Furthermore, large change of the slope can be seen like a green line at about 15 ps in Fig. 26. These deviations are thought to be a noise due to the statistically insufficient calculational conditions. If larger cell is used and calculation time is extended sufficiently, these lines will be linear and close.

The increase of MSD indicates the diffusion of O ions, therefore an order-disorder transition. However the MSD is the average of displacement of all O ions and not easy to see the change of the array in the O sublattice. Thus we investigated the arrays of every 100 MD step structures. The O sites in the 80 atoms cubic cell are distinguished by a grid based on fluorite structure; the cell was divided by 4×4×4 mesh and the array of each structure was determined. The number of jumps which the O ions need to across the grid to be its array from the initial position was counted. Therefore the number of jumps shows the deviation from the initial array. If the O ions hardly move and MSD does not increase, the number of jumps also does not increase. On the other hand, if the O ions diffuse significantly, the number of jumps also increases. After counting the number of jumps, it was expressed by the darkness of the color of a band. The region in which the number of jumps is 0 is the darkest and more than 10 is shown white. Figure 29 shows the schema of the band. In the white region, the array is considerably different from the initial array, therefore it can be considered that the transition from ordered phase to disordered phase has occurred. Figure 30-35 show the bands at each temperature. At 700 K, the initial array is maintained till the end of the examined time and the color of bands are dark. One of a band in c-η phase changes light color. This difference of the results is thought to come from the statistically insufficient conditions as described above. If we simulate longer time, the array might change and the color of top and bottom bands of c-η phase also change light in Fig. 30. At 800 K, the order-disorder transition can be seen in c-η and c-ε' phase. On the other hand, all the

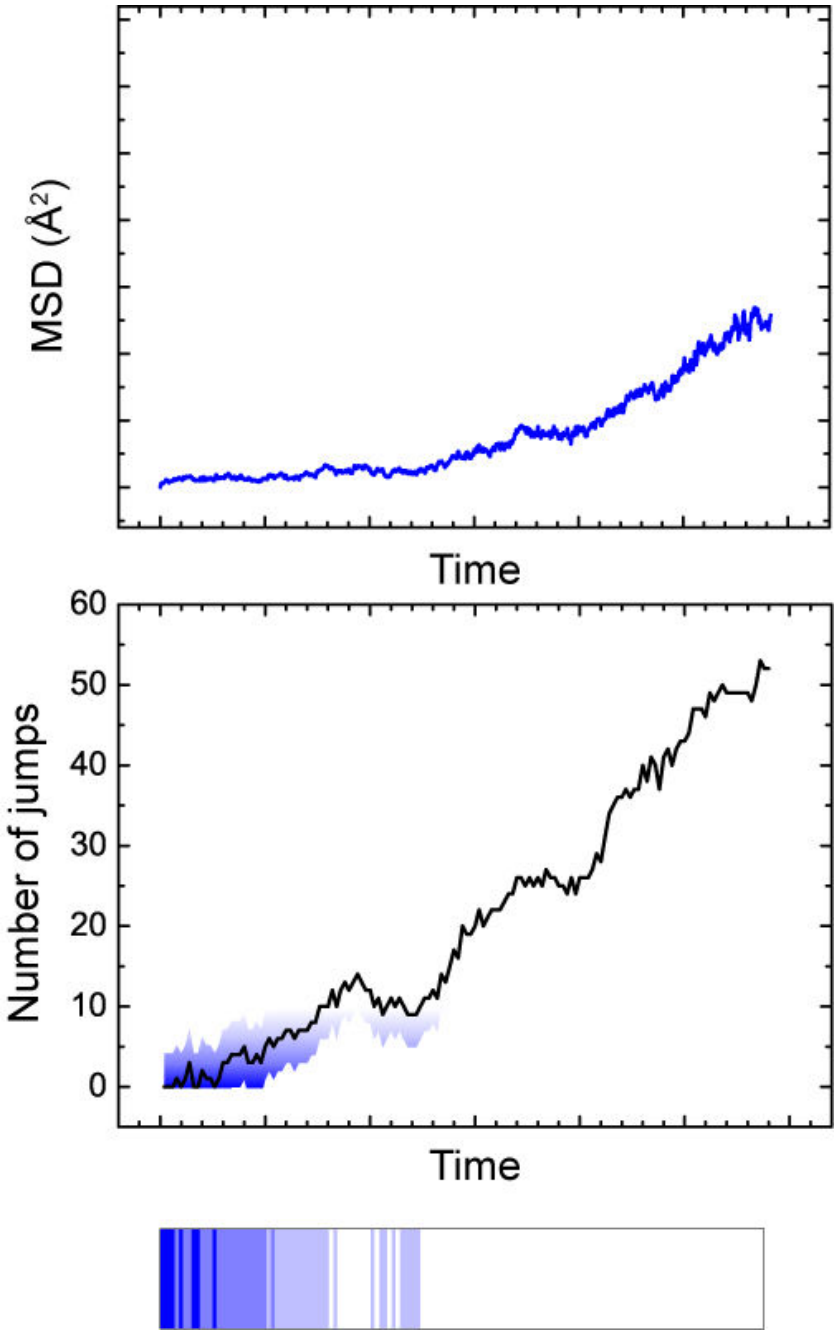

FIG. 29. The schema of the band which shows the deviation from the initial array. The region in which the number of steps is 0 is the darkest and more than 10 is shown white.

three bands of c-β phase show that the c-β phase is maintained till the end as shown in Fig. 31. At 900 K and 1000 K, the order-disorder transition appear earlier in c-η and c-ε' phase, but two of three bands of c-β are dark which mean the c-β phase does not change as shown in Fig. 32 and 33. At 1100 K, order-disorder transition can be seen for all the bands as shown in Fig. 34. At 1200 K, the difference of the bands between the three phases can not be seen and white region appears within 5 ps as shown in Fig. 35.

Figure 31-33 clearly shows that c-β phase is hard to change its array compared with the other structures. If the c-β phase is considered as the β-Bi_2O_3, this is consistent to the experimental report in which only δ-β phase transition has been observed so far. However, it should be noted that the formation energy of the three phases are almost the same. The energy of c-β phase is even slightly higher than that of c-η phase. Although the energies are almost the same, a difference can be seen in the structural features of c-β phase and c-η phase. In c-η phase (correspond to bixbyite-LS arrangement), ions distribute evenly and electrostatic energy is lower compared with c-β phase (correspond to <100>-LS arrangement) as shown in Fig. 22. On the other hand, the vacant sites are aligned in one direction and c-β phase forms molecular like structure. In these structures, energy is lowed by localizing electrons in the direction of vacant site as described in Part II. Such a structural feature might affect on the stability against order-disorder transition.

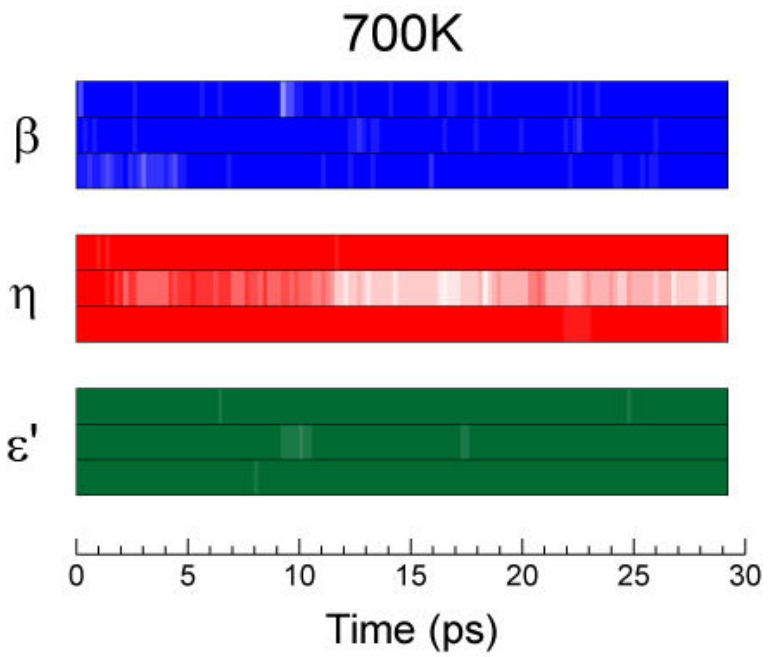

FIG. 30. The band which shows the deviation from initial O atomic array at 700 K.

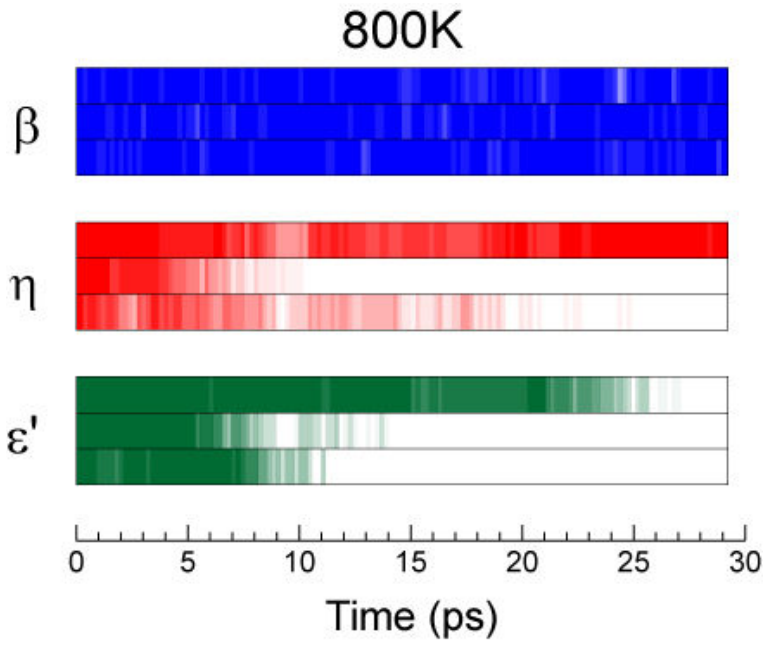

FIG. 31. The band which shows the deviation from initial O atomic array at 800 K.

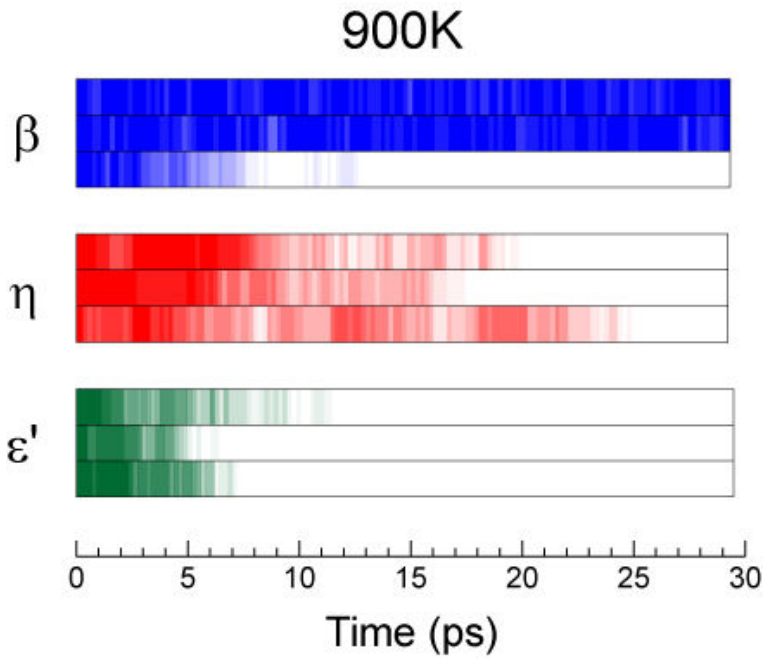

FIG. 32. The band which shows the deviation from initial O atomic array at 900 K.

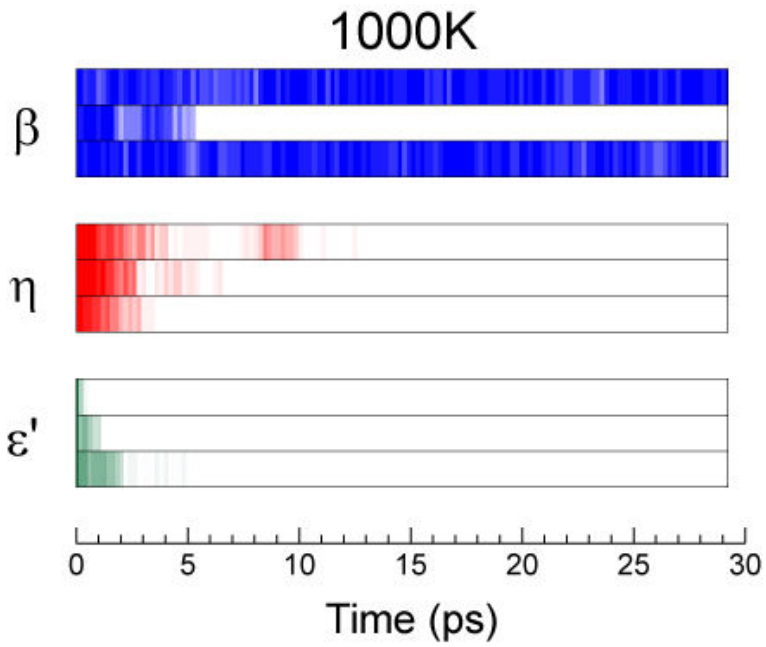

FIG. 33. The band which shows the deviation from initial O atomic array at 1000 K.

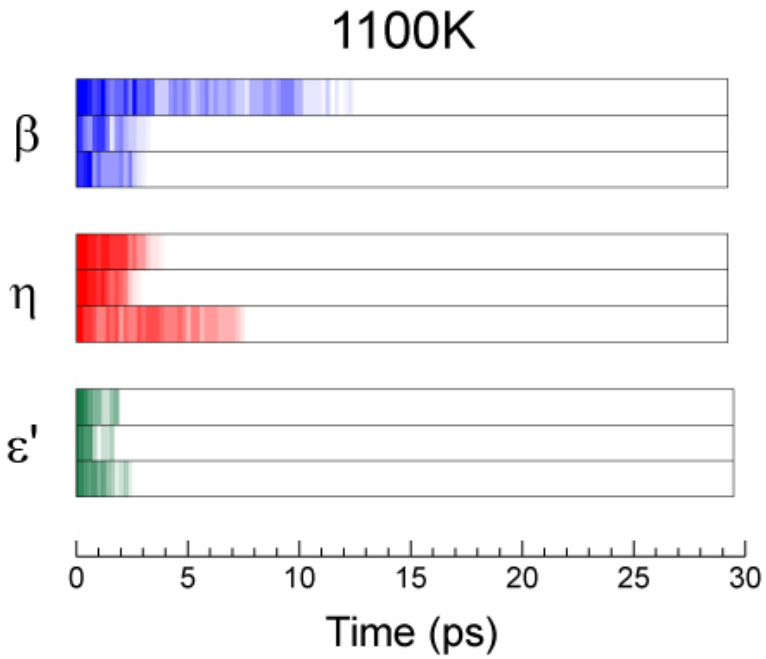

FIG. 34. The band which shows the deviation from initial O atomic array at 1100 K.

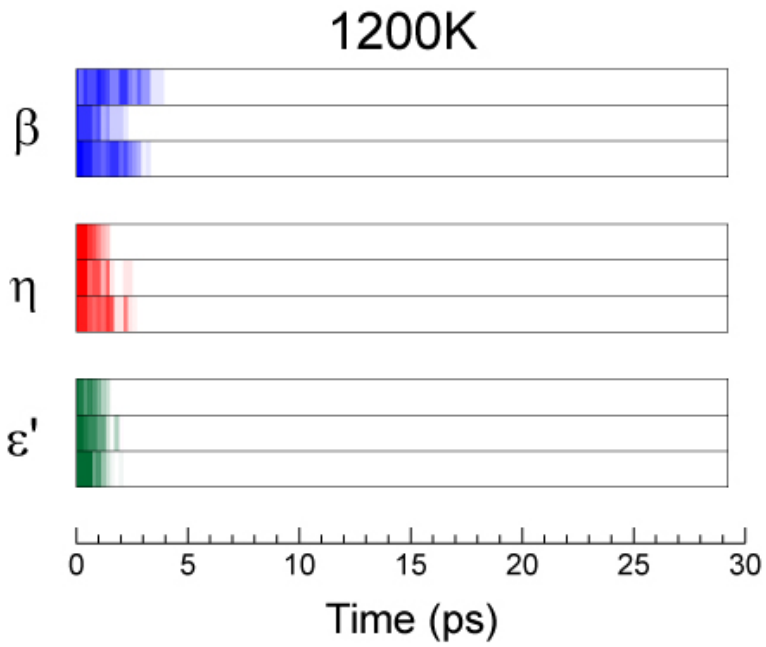

FIG. 35. The band which shows the deviation from initial O atomic array at 1200 K.

B. Diffusion of bismuth ions

Similarly to O ions, the MSD of Bi ions is investigated. Figure 36 shows the MSD of Bi ions at 1200 K. As can be seen in Fig. 36, Bi ions hardly move and MSD is almost 0 for all phases even at 1200 K. We performed MD calculation on c-β phase at 1500 K but Bi ions still do not move. This result is significantly different from the experimental report in which the melting point of Bi_2O_3 is reported as about 1100 K.[13] In general, the volume of solid expand as the temperature increase and volume change can be also seen at melting. In the case of alkali halide, the volume expansion with melting is about 10-30 %.[14] However, we used a lattice constant calculated by the first-principles calculations which provide the value at 0 K. In the current simulations the volume is fixed during the calculations therefore such a volume expansion is not considered. Thus the fixed volume is thought to make a constraint for the melting of Bi ions. To ease the constraint of the volume, additional MD calculation was done with larger cell. The new initial structure with the larger lattice constant by 2 %, 4 % and 8 % is constructed based on c-β phase. MD calculations are done for each structure once at 1500 K. Figure 37 shows the MSD of Bi ions in the expanded c-β phase at 1500 K. Bi ions still do not diffuse in the 2 % larger cell. However, they start diffusing at about 10 ps later in the 4 % larger cell. In the 8 % larger cell, Bi ions start diffusing at the beginning of the simulation. This diffusion of Bi ions corresponds to the melting of Bi_2O_3. We did the same calculations at 1100 K but no significant diffusion of Bi ions can be seen. Although thus it is difficult to match the experimental and calculational melting point, it is indicated that the volume expansion facilitates the diffusion of Bi ions.

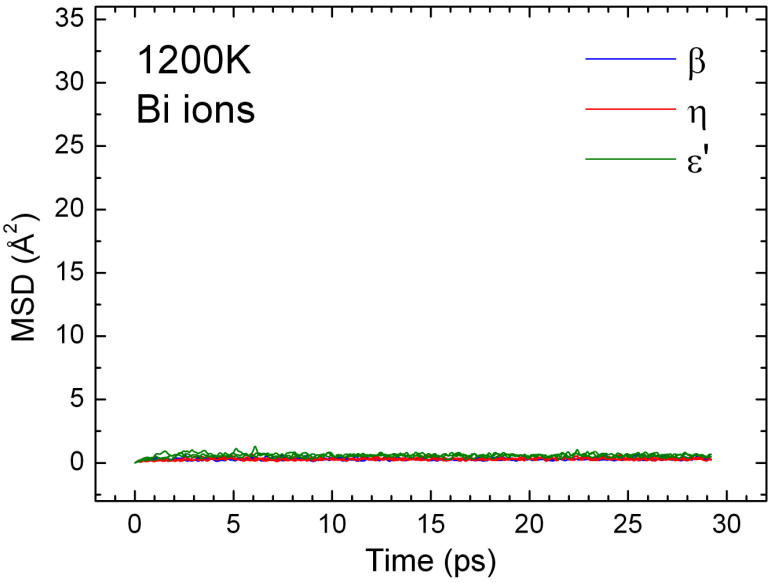

FIG. 36. The mean square displacement of Bi ions at 1200 K. Blue, red and green lines correspond to c-β, c-η and c-ε', respectively.

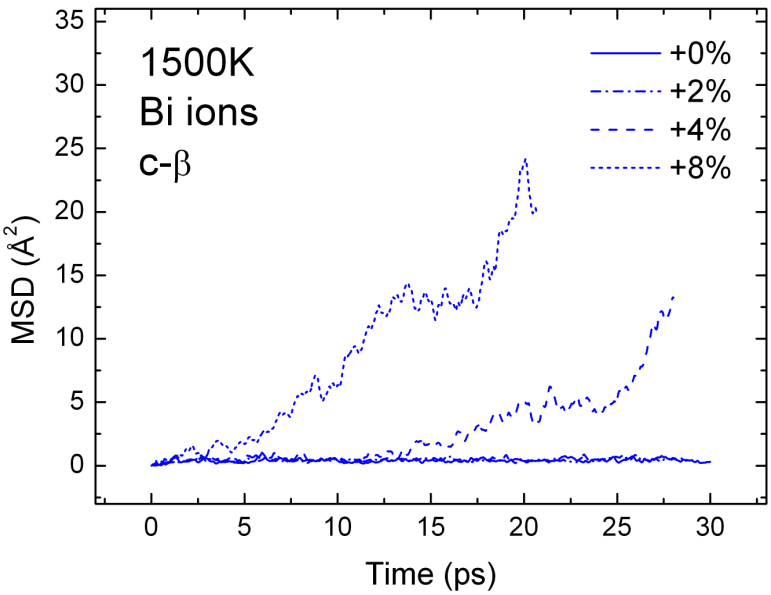

FIG. 37. The mean square displacement of Bi ions in c-β with larger lattice constant at 1500 K.

4. DISCUSSION

A. Diffusion coefficient

After the transition to disordered phase, c-β, c-η and c-ε' phases can be considered as disordered δ-Bi_2O_3. In this section, we calculate the self-diffusion coefficient of δ-Bi_2O_3. The self-diffusion coefficient, D^O, is given by

$$D^O = \lim_{t\to\infty} \frac{\mathrm{MSD}}{6t}$$

where, MSD is the mean square displacement and t is time. Although the calculational condition is statistically insufficient and each structure is not equilibrium state, it can be thought the slope of the MSD does not change so much even at an appropriate calculational condition. Thus we estimated the self-diffusion coefficient of δ-Bi_2O_3 roughly at each temperature higher than 800 K. Since the O ions do not diffuse in a part of simulations of c-β phase, D^O of c-β is also estimated. Figure 38 shows the average of D^O of δ-Bi_2O_3 and c-β at each temperature. D^O of δ-Bi_2O_3 at 1000 K is 7×10^{-6} cm^2/s which is consistent to the other ionic conductors.

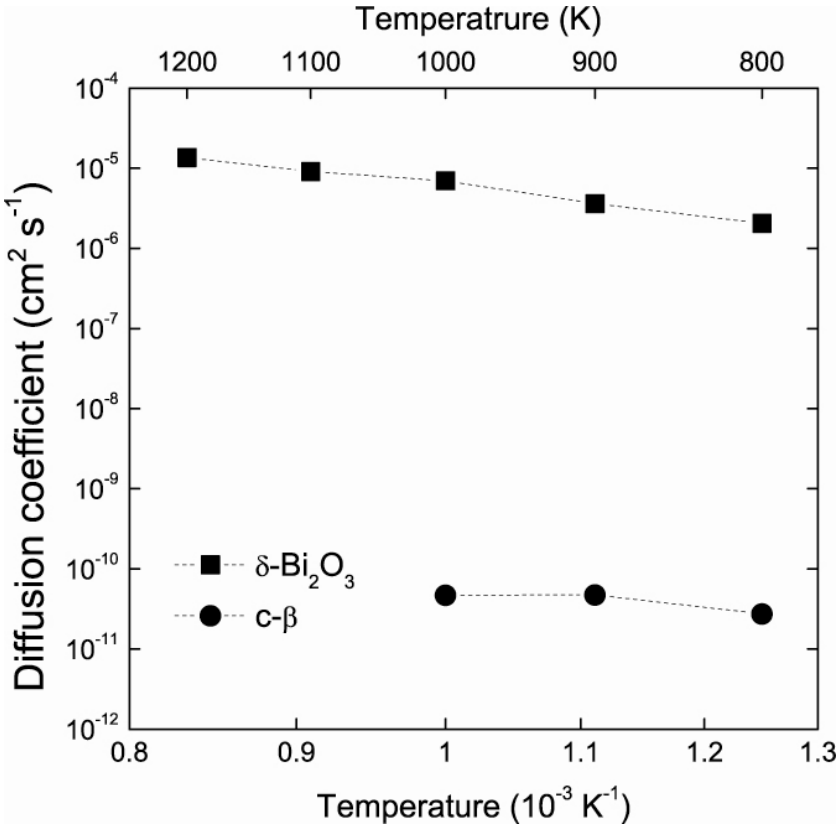

FIG. 38. The average of diffusion coefficient, D^O of δ-Bi_2O_3 and c-β phase at each temperature.

B. The oxygen ionic diffusion in larger cell

As described in Part I, only δ-Bi_2O_3 shows high oxide ionic conductivity and various investigations have been examined to stabilize δ-Bi_2O_3. On cooling δ-Bi_2O_3, tetragonal β phase which is considered one of an ordered df-Bi_2O_3 appears with the considerable decrease of the ionic conductivity. If this ordering of O ions can be prevented, as is said the order-disorder transition temperature can be lowered, high ion-conduction phase, δ-Bi_2O_3, might be maintained at lower temperature. In the section 3-A, it was shown that c-β phase is more stable than c-η and c-ε' phase and the O ions

in c-β do not diffuse at 800 K. Thus we aimed to make c-β phase disordered at 800 K.

In the past research, the relation between lattice parameter and ionic conductivity is discussed for Li ions in garnet-like $Li_5La_3Ta_2O_{12}$ system[15] or for O ions in a pyrochlore-type composition, $(Y_{1-x}La_x)_2(Ce_{1-x}Zr_x)_2O_7$ and $(Nb_{1-x}Yb_x)_2(Ce_{1-x}Zr_x)_2O_7$ system.[16] They showed ionic conductivity increase as the volume of the cell expand. It was also shown in section 3-B that the diffusion of Bi ions can be facilitated by enlarging lattice parameter. Therefore we performed MD calculations on c-β phase with a larger lattice parameter to examine the disordering in the oxygen sublattice at lower temperature.

Figure 39 shows the MSD and the deviation from the initial array of the oxygen sublattice in the c-β phase with the original lattice parameter and larger lattice parameter by +4% and +8%. In the original and 4 % larger cell, no O ionic diffusion can be seen. However, the top of the band of 8% larger cell shows order-disorder transition. The bottom of the band also shows the change of array. It indicates the diffusion of O ions is also promoted by volume expansion. The diffusion of Bi ions is also investigated but no diffusion can be seen in these larger cells. Therefore, it is thought that expansion the volume is efficient to lower the order-disorder transition temperature, that is, maintain the disordered phase, δ-Bi_2O_3.

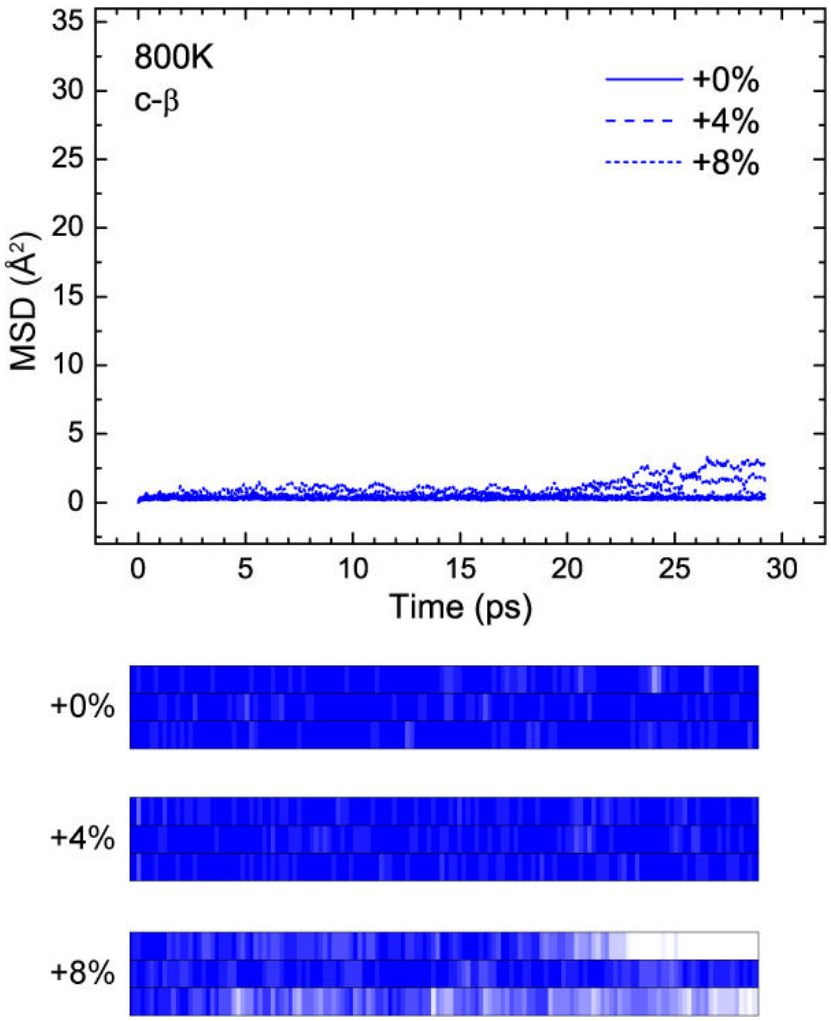

FIG. 39. The MSD and the band which shows the deviation from the initial arrangement of O ions in larger cell of c-β.

C. Sulfur doped system

It was shown that ionic diffusion is promoted by expanding the volume. In the previous section, the lattice parameter is changed artificially in the calculations. As a simple way to enlarge cell volume, larger ions are often substituted. Actually, various dopants have been substituted into Bi_2O_3 to maintain the high ionic conductivity at lower temperature and some of them made a success. The most of the previous report on doped systems discuss a cation doped system.[17-21] However, the ionic radius of Bi is quite large and it is difficult to enlarge the lattice parameter by replacing Bi ions. The previous doped systems, including larger cations (e.g; La) doped system, seems to succeed in stabilizing ion-conduction phase by another effect. On the other hand, the number of research on anion doped system is few. Therefore, we substituted S ions into the oxygen sublattice as a larger anion.

The new initial structures were constructed by replacing one, four and eight O ions by S ions in c-β phase. Firstly, several high symmetric array models for each composition were optimized with its cell volume and atomic coordinate allowed to relax. Secondly, the lowest energy structure for each composition was changed into cubic with the same volume and optimized its atomic coordinate. Hereafter we call the one, four and eight O ions replaced structure c-β-S0.02, c-β-S0.08 and c-β-S0.17, respectively. The figure after the "S" corresponds to the composition of S. The lattice parameter and formation energy based on c-β phase and Bi_2S_3 of each structure is shown in Table 12. As can be seen in Table 12, lattice parameter of c-β can be enlarged by 0.6 %, 1.7 % and 4.1 % in c-β-S0.02, c-β-S0.08 and c-β-S0.17, respectively. Assuming the ideal solution, the entropy is given by $\Delta S = -k_B (x \ln x + (1 - x) \ln (1-x))$, where k_B is the Boltzmann constant and x is the composition of S. At 800 K the entropy term, $T\Delta S$ is 0.02, 0.06 and 0.09 eV/f.u. for c-β-S0.02, c-β-S0.08 and c-β-S0.17, respectively. Therefore, although

the formation energy is positive, they can be synthesized by the effect of entropy except for c-β-S0.02.

MD calculations were done for these structures under the same condition of undoped system. Figure 40 shows the MSD and the deviation from initial array of oxygen sublattice in the doped systems at 800 K. Undoped c-β or c-β-S0.02 does not change its array at 800 K. On the other hand, the diffusion of O ions can be seen in c-β-S0.08 and c-β-S0.17. Although the lattice parameter of c-β-S0.08 is smaller than that of 4 % larger c-β in which the O ions do not diffuse at 800 K, the band indicates that the O ions can diffuse in c-β-S0.08 at that temperature. Thus other interaction than volume expansion should promote the diffusion of O ions.

It is indicated that c-β phase can be get disordered at lower temperature by doping sulfur, which leads the maintaining δ phase at lower temperature. However, it is found that S ions or Bi ions also move in the doped system. Figure 41 and 42 shows the MSD of S ions and Bi ions in sulfur doped system at 800 K. Since the number of S ions is few, the MSD which is the average of displacement fluctuate largely in Fig. 41. A large displacement of S ions can be seen even in c-β-S0.02. Since oxide ionic conductor should pass only O ions, the diffusion of S ions is not desirable. It seems that too much doping sulfur make the Bi sublattice unstable as shown in Fig. 42. Although substituting sulfur is thought to be efficient for promoting diffusion of O ions, there are other problems to improve for applying Bi_2O_3 to an oxygen ionic conductor.

TABLE 12. The lattice parameter and formation energy based on c-β and Bi_2S_3 of c-β-S0.02, c-β-S0.08 and c-β-S0.17.

	c-β-S0.02	c-β-S0.08	c-β-S0.17
Lattice Parameter (Å)	11.47	11.60	11.86
The Ratio of Lattice Parameter (%)	+0.6	+1.7	+4.1
Formation Energy (eV/f.u.)	0.03	0.05	0.08

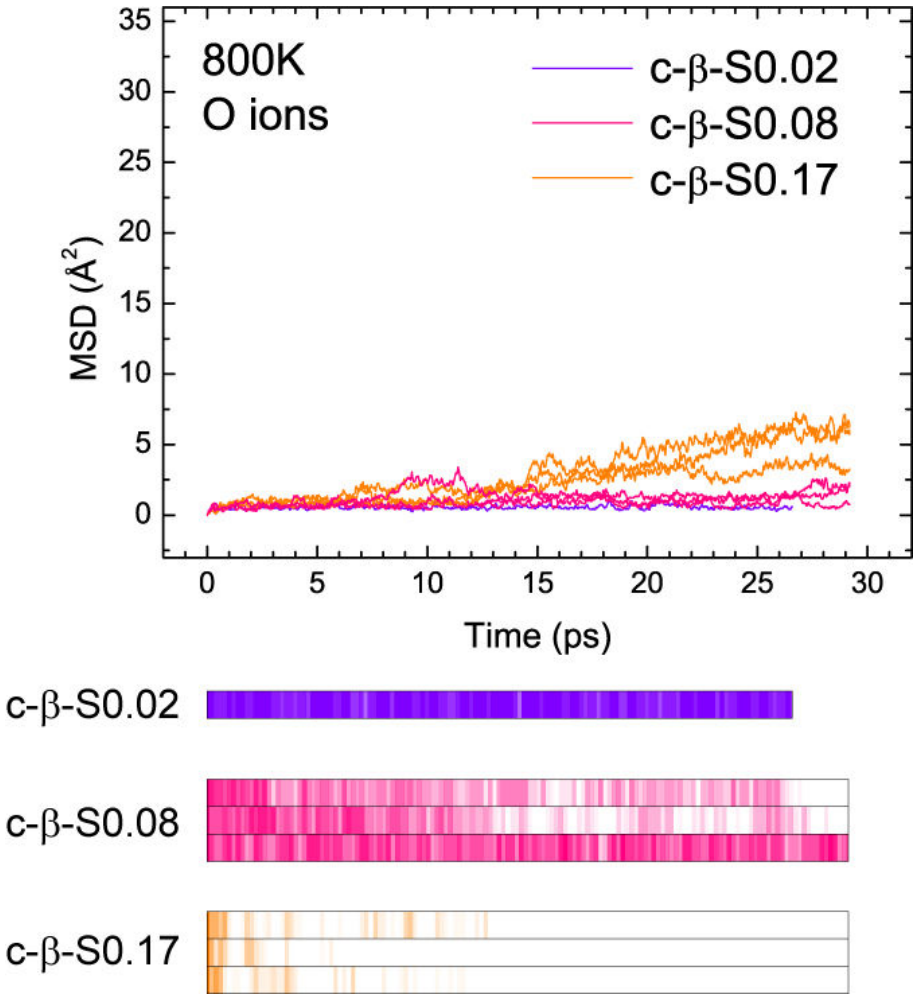

FIG. 40. The MSD and the band which shows the deviation from the initial arrangement of O ions in sulfur doped c-β phase.

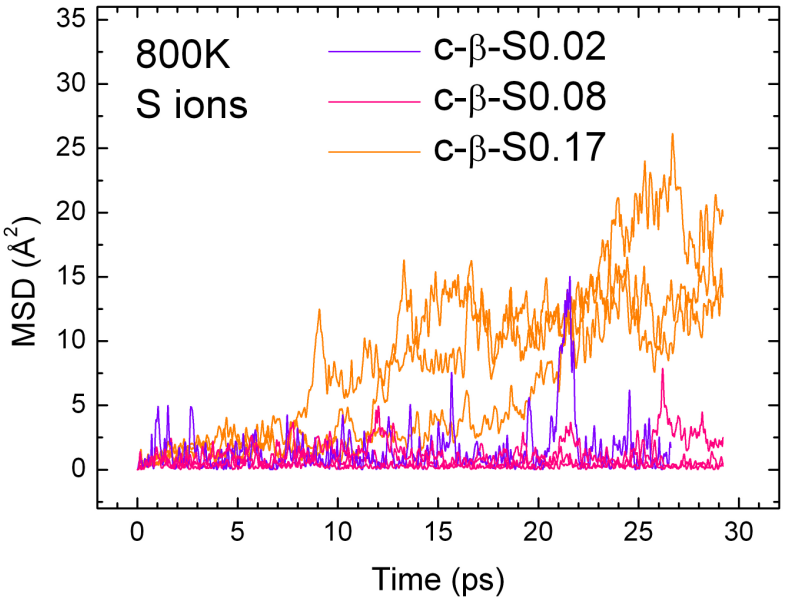

FIG. 41. The MSD of S ions in sulfur doped c-β phase.

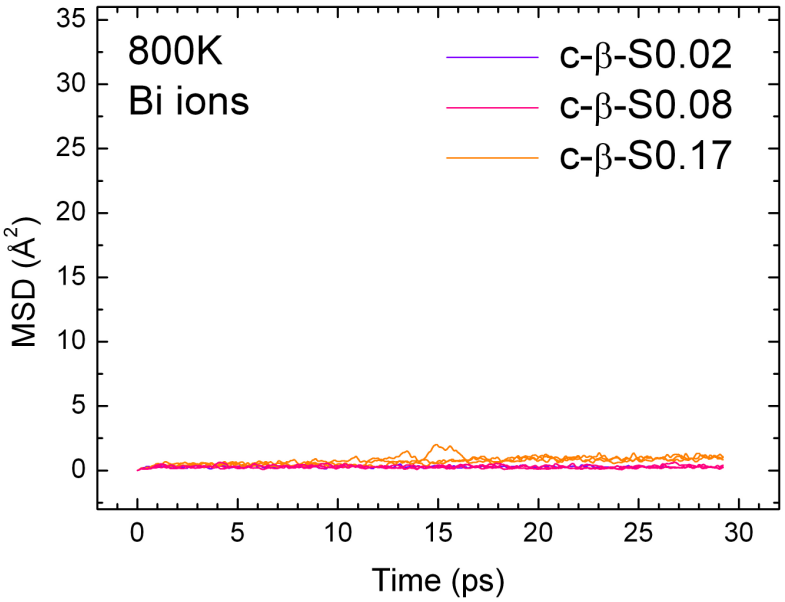

FIG. 42 The MSD of Bi ions in sulfur doped c-β phase.

5. SUMMARY

In order to see the movement of O ions in df-Bi_2O_3, first-principles calculations were performed for the three models, c-β, c-η and c-ε'. The major results of this study can be summarized as follows:

1) O ions hardly diffuse at 700 K in all phases. O ions in c-η and c-ε' start diffusing but c-β phase is maintained at 800 K. Two of three calculations showed that c-β phase is maintained even at 1000 K. As the temperature increase, order-disorder transition can be seen earlier. It was shown that c-β is more stable than other df-Bi_2O_3, which is consistent to that only δ-β transition has been observed so far.

2) Bi ions hardly move even at 1500 K which is inconsistent to the experimentally report in which the melting point of Bi_2O_3 is reported as about 1100 K. This discrepancy comes from that we did not consider the volume expansion. Bi ions diffused at 1500 K when we c-β with 4 % larger lattice parameter. However, no diffusion could be seen at 1100 K.

3) Self-diffusion coefficient of δ-Bi_2O_3 is roughly estimated with the MSD. The Diffusion coefficient of δ-Bi_2O_3 at 1000 K was 7×10^{-6} cm^2/s which is consistent to the other ionic conductors.

4) It was indicated that expanding volume promotes O ionic diffusion. Although no O ionic diffusion could be seen in c-β at 800 K, an order-disorder transition could be seen in a larger cell with 8 % larger lattice parameter.

5) In order to expand the volume and stabilize the disordered phase at lower temperature, sulfur doped system was suggested. The lattice parameter could be enlarged by substituting sulfur into oxygen sites. With this expansion, the O ionic diffusion could be seen in c-β phase at lower temperature. However, S ions also diffuse in the dope system which is not desirable for applications.

References

[1] M. S. Khan, M. S. Islam and D. R. Bates, J. Mater. Chem. **8,** 2299 (1998)

[2] C. A. J. Fisher and H. Matsubara, Solid State Ionics **113-115,** 311 (1998)

[3] F. Pietrucci, M. Bernasconi, A. Laio and M. Parrinello, Phys. Rev. B **78,** 094301 (2008)

[4] P. W. M. Jacobs and D. A. MacDónaill, Solid State Ionics **23,** 279 (1987)

[5] D. S. Aidhy, J. C. Nico, S. B. Sinnott, E. D. Wachsman, and S. R. Phillpot, J. Am. Ceram. Soc. **91,** 2349 (2008).

[6] D. S. Aidhy, S. B. Sinnott, E. D. Wachsman and S. R. Phillpot, Ionics, **16**, 297 (2010)

[7] C. E. Mohn, S. Stølen, S. T. Norberg, and S. Hull, Phys. Rev. B **80,** 024205 (2009).

[8] G. Kresse and J. Hafner, Phys. Rev. B **47**, R558 (1993).

[9] G. Kresse and J. Furthmüller, Phys. Rev. B **54**, 11169 (1996).

[10] G. Kresse and J. Furthmüller, Comput. Mater. Sci. **6**, 15 (1996).

[11] P. Blöchl, Phys. Rev. B **50**, 17953 (1994).

[12] J. P. Perdew, K. Burke, and M. Ernzerhof, Phys. Rev. Lett. **77**, 3865 (1996).

[13] H. A. Harwig and A. G. Gerards, Thermochim. Acta **28,** 121 (1979).

[14] K. Furukawa, Discuss. Faraday Soc., **32,** 53 (1961).

[15] R. Murugan, V. Thangadurai and W. Weppner, J. Electrochem. Soc. **155**, A90 (2008).

[16] H. Nishino, H. Yamamura, T. Arai, K. Kakinuma, K. Nomura, J. Ceram. Soc. Jpn. **112**, 541 (2004).

[17] N. M. Sammes, G. A. Tompsett, H. Näfe, and F. Aldinger, J. Eur. Ceram. Soc. **19,**

1801 (1999).

[18] M. Drache, P. Roussel, and J. Wignacourt, Chem. Rev. **107,** 80 (2007).

[19] C. Michel, V. Caignaert and B. Raveau, J. Solid State Chem. **90,** 296 (1991)

[20] E. D. Wachsman, S. Boyapati and M. J. Kaufman, J. Am. Ceram. Soc. **83,** 1964 (2000)

[21] C. Weng and W. J. Wei, J Am. Ceram. Soc. **93,** 3124 (2010)

Part V
General conclusion

The structure and relationship between polymorphs of bismuth oxide, Bi_2O_3, was systematically investigated by first-principles calculations.

In Part II, A series of dynamically stable structures of the defective fluorite-Bi_2O_3 is found by first-principles lattice dynamics calculations. The crystal symmetry is lowered and local distortion is included systematically along imaginary modes of lattice vibrations. A clear band gap appears when local distortion is included in this way, which is consistent with experimental results. Many theoretical calculations in the past indicated metallic or semimetallic electronic structures. The appropriate inclusion of the symmetry breaking and local distortion are therefore essential in reproducing the electronic structures of Bi_2O_3. The three stable structures are found to have an energy of 0.07 to 0.08 eV/formula-unit relative to α-Bi_2O_3. The arrays of oxide-ion vacancies in two of these structures are the same as those of β-Bi_2O_3 and ε-Bi_2O_3, which were experimentally identified as stable phases. A bixbyite-type vacancy-array structure is also found to be another stable phase in the present study, which is named η-Bi_2O_3. It is suggested that the three stable structures of Bi_2O_3 are ordered low-temperature polymorphs of the disordered δ-Bi_2O_3 in the defective fluorite-Bi_2O_3 family.

In Part III, the relationships between atomic arrangements, electronic structures and energetics of three sesquioxides, i.e., As_2O_3, Sb_2O_3, and Bi_2O_3 are systematically investigated by sets of first-principles lattice-dynamics calculations. Dynamically stable structures of defective fluorite family are searched by including atomic displacements along imaginary modes of lattice vibrations that appear in highly symmetric defective

fluorite structures. Experimentally reported crystal structures (arsenolite-As_2O_3, α-Sb_2O_3, β-Sb_2O_3, β-Bi_2O_3) are found to be made by the symmetry breaking and the local atomic distortion in this way. Some dynamically stable structures as yet-unknown by experiments are discovered. In the dynamically stable low symmetry structures, valence electrons localize and form asymmetric charge distribution along the direction of an empty anion-site of the defective fluorite structure. This is the common characteristic of "lone pair". The origin of the large distortions in the three sesquioxides cannot be explained by a simple electrostatic picture. Detailed analysis of the electronic structures by taking account the symmetry breaking, local distortion and the formation of lone pair are essential for discussing the relation between structures, stability and properties in these sesquioxides.

In Part IV, first-principles MD calculations were performed on the three stable models, c-β, c-η and c-ε' phase to see the movement of O ions and transition from ordered phase to disordered phase in df-Bi_2O_3. The disordering in the oxygen sublattice could be seen at about 800 K. Although the formation energy is almost the same in these structures, c-β phase maintained its array at higher temperature compared with c-η and c-ε' phase. This is consistent to the experimental report in which only δ-β transition has been observed so far. It was shown that the ionic diffusion is promoted by expansion of volume. In order to obtain the disordered phase at lower temperature, sulfur doped system was suggested. Although O ions hardly diffuse in c-β phase at 800 K, the sulfur doped c-β phase showed order-disorder transition at that temperature. However, it was shown that S ions also move in the sulfur doped system.

ACKNOWLEDGMENTS

The author would like to express his deepest gratitude to Professor Isao Tanaka at Kyoto University for continuous guidance and encouragement throughout this work. The author wishes to express his gratitude to Associate Professor Katsuyuki Matsunaga for helpful discussions and advices. He would like to thank Associate Professor Fumiyasu Oba for his continuous helpful discussions and advices. The author gratefully shows his appreciation to Associate Professor Yukinori Koyama for his helpful discussions and fruitful advices about how to live as a scientist throughout this work. The author would like to express his deepest gratitude to Associate Professor Atsuto Seko for his timely advices and discussion throughout this work. He would like to express his deepest gratitude to Professor Akira Sakai and Hiroyuki Nakamura for their critical reading of this thesis.

The author would like to thank to Associate Professor Masato Yoshiya at Osaka University for the information about BMEA2010 which encouraged the MD calculations. The author sincerely acknowledges Dr. Akihide Kuwabara at Japan Fine Ceramics Center for his generous help when the author started this work. The author would like to express deepest gratitude to Dr. Atsushi Togo for his fruitful advices for the lattice dynamics calculations. He wishes to express his gratitude to Dr. Tetsuya Tohei at Tokyo University for his help for the test calculations of lattice dynamics. The author would like to thank Dr. Hidekazu Ikeno for his kind advice. The author would like to appreciate Associate Professor Koretaka Yuge for his timely advices for the calculations of cluster expansion. The author would like to express his deepest gratitude to Dr. Kazuaki Toyoura for his fruitful discussions and advices.

The author sincerely acknowledges Dr. Yu Kumagai for his help and encouragement in the laboratory life. He would like to thank Dr. Hiroyuki Hayashi for

his helpful advices from the experimental view. He wishes to express his gratitude to Dr. Yuji Otsuka for his help and encouragement. The author would like to thank Mr. Minseok Choi, Mr. Hidenobu Murata and Mr. Yuji Takahashi for their advices and encouragement in the laboratory life.

The author wishes to make grateful acknowledgement to the members of Professor Tanaka's group for helpful discussions throughout this work. Especially, he would like to thank Ms. Makiko Orita for her arrangement of various things.

Finally, the author would like to sincerely thank his family for their enduring support and encouragement.